Geol. Mag. **150** (*1*), *2013, pp. 50–71. © Cambridge University Press 2012*
doi:10.1017/S0016756812000283

Geochemistry, petrogenesis and tectonic implications of granitic plutons at the Liziyuan orogenic goldfield in the Western Qinling Orogen, central China

TAO YANG, LAIMIN ZHU*, FEI WANG, HUJUN GONG & RUKUI LU

State Key Laboratory of Continental Dynamics, Department of Geology, Northwest University, Xi'an 710069, China

(*Received* 21 August 2011; *accepted* 28 March 2012; *first published online* 29 June 2012)

Abstract – The Liziyuan goldfield is located along the northern margin of the western part of the Qinling Orogen (WQO). The goldfield consists of five gold-only deposits hosted by metavolcanic rocks, and one polymetallic (Au–Ag–Pb) deposit hosted by the Tianzishan Monzogranite. As the Liziyuan goldfield appears to be spatially and temporally related to the Jiancaowan Porphyry, the study of the deposit provides a crucial insight into the relationship between tectonic-magmatic events and gold metallogenesis in the WQO. In this paper, we present whole-rock major and trace element geochemistry, and *in situ* zircon U–Pb and Lu–Hf isotopic data from the Tianzishan Monzogranite and Jiancaowan Porphyry. The two granitic plutons are enriched in LILEs and LREEs, depleted in HFSEs and have zircon $\varepsilon_{Hf}(t)$ values between −14.1 and −5.1 for the Tianzishan Monzogranite and between −21.0 and −8.4 for the Jiancaowan Porphyry. These characteristics indicate that the granites are derived from the crust. The Tianzishan Monzogranite has LA-ICP-MS zircon U–Pb ages of 256.1 ± 3.7 to 260.0 ± 2.1 Ma, which suggests that it was emplaced in the WQO during the convergence of the North and South (Yangtze) China cratons in the early stage of the Qinling Orogeny. In contrast, the porphyry has a LA-ICP-MS zircon U–Pb age of 229.2 ± 1.2 Ma, which is younger than the peak collision age, but corresponds to the widespread Late Triassic post-collisional granitic plutons in the WQO. The Tianzishan Monzogranite has somewhat higher Sr contents (196–631 ppm), lower Y (2.23–19.6 ppm) and Yb (0.20–2.01 ppm) contents, and a positive Eu/Eu* averaging 1.15. These characteristics suggest the pluton was derived from partial melting of the thickened crust. In contrast, the relatively higher MgO content (0.85–2.08 wt %) and Mg no. (43.4–58.2) of the Jiancaowan Porphyry indicates that insignificant amounts of subcontinental lithospheric mantle-derived mafic melts were involved in the generation of the magma. The Liziyuan goldfield is hosted by faults in greenschist-facies metamorphic rocks. Fluid inclusion studies suggest that gold was precipitated from CO_2-rich, low-salinity and medium temperature fluids. This feature is consistent with the other orogenic gold deposits throughout the world. The field relationships and zircon U–Pb ages of the two granitic plutons suggest that gold mineralization is coeval with or slightly younger than the emplacement of the Jiancaowan Porphyry. Therefore, both the porphyry and deposit formed during the post-collisional stage of the Qinling Orogen.

Keywords: Liziyuan goldfield, LA-ICP-MS U–Pb dating, zircon Hf isotopes, Western Qinling Orogen.

1. Introduction

The Triassic Western Qinling Orogen (WQO) is one of the most important gold producing regions in China (Mao *et al*. 2002; Zhou, Goldfarb & Phillips, 2002; Zeng *et al*. 2012). During the last three decades, many gold deposits have been discovered in the region, including the giant Yangshan (308 t Au), the world-class Baguamiao and Jinlongshan, the large Liba, Luerba, Zhaishang, Dongbeizhai, Dashui and Ma'anqiao, and numerous small gold deposits. The WQO is a tectonic-magmatic belt with abundant intermediate to felsic plutons (Sun *et al*. 2002; Zhang *et al*. 2005; Zhang, Wang & Wang, 2008; Gong *et al*. 2009; Qin *et al*. 2009, 2010; Jiang *et al*. 2010; Zhu *et al*. 2011). The plutons are close to lode (orogenic) gold deposits in the region (Mao *et al*. 2002; Chen *et al*. 2004; Yang *et al*. 2006; Zhu *et al*. 2010). Zhang *et al*. (2009) and Yin & Yin (2009) proposed that these gold deposits should be grouped into the class of granite-related gold deposits (i.e. the gold mineralization is genetically related to the granite), but orogenic gold deposits are proximal to granites throughout the world (e.g. Groves *et al*. 2003; Goldfarb *et al*. 2005; Duuring, Cassidy & Hagemann, 2007).

Feng *et al*. (2002, 2004) and Zhang & Mao (2004) proposed that gold metallogenesis in the WQO is associated with magmatic-hydrothermal fluids based on the isotopic data of proposed ore-forming fluids carrying the metal. Other authors argued that the ore-forming fluids are dominated by metamorphic fluids produced by the orogenesis during the Qinling Orogen (Mao *et al*. 2002; Chen *et al*. 2004; Li *et al*. 2008; Zhu *et al*. 2009*b*; Zhou *et al*. 2011). Based on geochronological and geochemical studies, it has also been suggested that the granites pre-date, and hence did not contribute to, gold mineralization (Yang *et al*. 2006; Zhu *et al*. 2009*b*, 2010), but it is also known that

*Author for correspondence: zhulaimin@nwu.edu.cn

https://doi.org/10.1017/S0016756812000283 Published online by Cambridge University Press

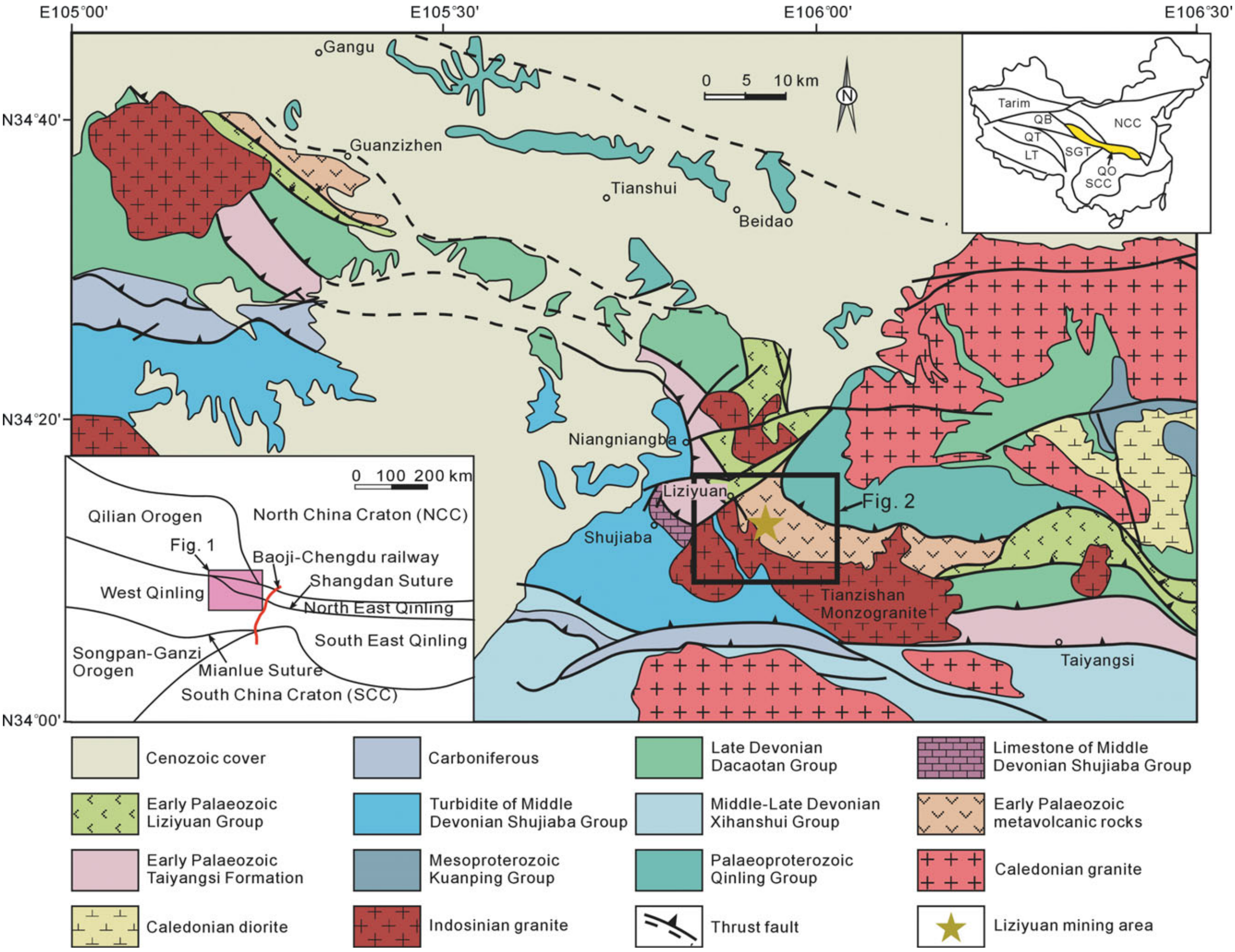

Figure 1. (Colour online) Regional geological map of the Liziyuan goldfield (modified after Pei *et al*. 2006). NCC – North China Craton; SCC – South China Craton; SGT – Songpan-Ganzi Terrane; QB – Qaidam Basin; QT – Qiangtang Terrane; LT – Lhasa Terrane; and QO – Qinling Orogen.

gold mineralization often follows the solidification of granites (Pirajno & Bagas, 2008).

The Liziyuan goldfield is located near the Jiancaowan Porphyry and Tianzishan Monzogranite along the northern margin of the WQO and is still in the exploration stage with an inferred resource of 30 t Au (Liu *et al*. 2011; Figs 1, 2). Hence, precise and accurate ages for the plutons can provide useful insights into the relationship between regional tectonic magmatism and gold mineralization in the orogen. In this paper, we present new whole-rock major and trace element geochemistry and *in situ* zircon U–Pb and Lu–Hf isotopic data for the Tianzishan Monzogranite and Jiancaowan Porphyry.

2. Regional geology

The Qinling Orogen, Qilian Orogen to the west and the Dabie–Sulu Ultra High Pressure (UHP) Zone to the east separate the North and South China cratons in central China (Fig. 1). The suturing of the cratons culminated during the Early Triassic Indosinian Orogeny with the northward subduction of the South China Craton beneath the North China Craton (e.g. Hacker *et al*. 1998; Meng & Zhang, 1999; Zheng *et al*. 2010). This collisional event was protracted, starting in the east within the Dabie–Sulu UHP Zone and culminating in the west within the Qinling Orogen in a progressive process event called 'scissor suturing' (Zhu *et al*. 1998; Zhang *et al*. 2004; Chen *et al*. 2006).

Field studies of the Qinling Orogen have identified suture zones that divide the orogen into the North Qinling Terrane and South Qinling Terrane via the Shangdan Suture (Meng & Zhang, 1999; Zhang *et al*. 2001; Dong *et al*. 2011). The South Qinling Terrane is further subdivided into the West and East Qinling domains approximately at the Baoji–Chengdu Railway along the Cenozoic Chengxian–Huixian Basin (Fig. 1; Zhang, Zhang & Dong, 1995; Zhang *et al*. 2001, 2007; Zheng *et al*. 2010). The southern boundary of the Qinling Orogen is also a suture known as the Mianlue Suture that separates the orogen from the South China Craton (Meng & Zhang, 1999; Zhang *et al*. 2001; Dong *et al*. 2011).

The Shangdan Suture is interpreted to have formed following subduction of the Shangdan Ocean during Early Silurian time (457–422 Ma; Qiu & Wijbrans, 2006; Mao *et al*. 2008*b*; Dong *et al*. 2011). The

https://doi.org/10.1017/S0016756812000283 Published online by Cambridge University Press

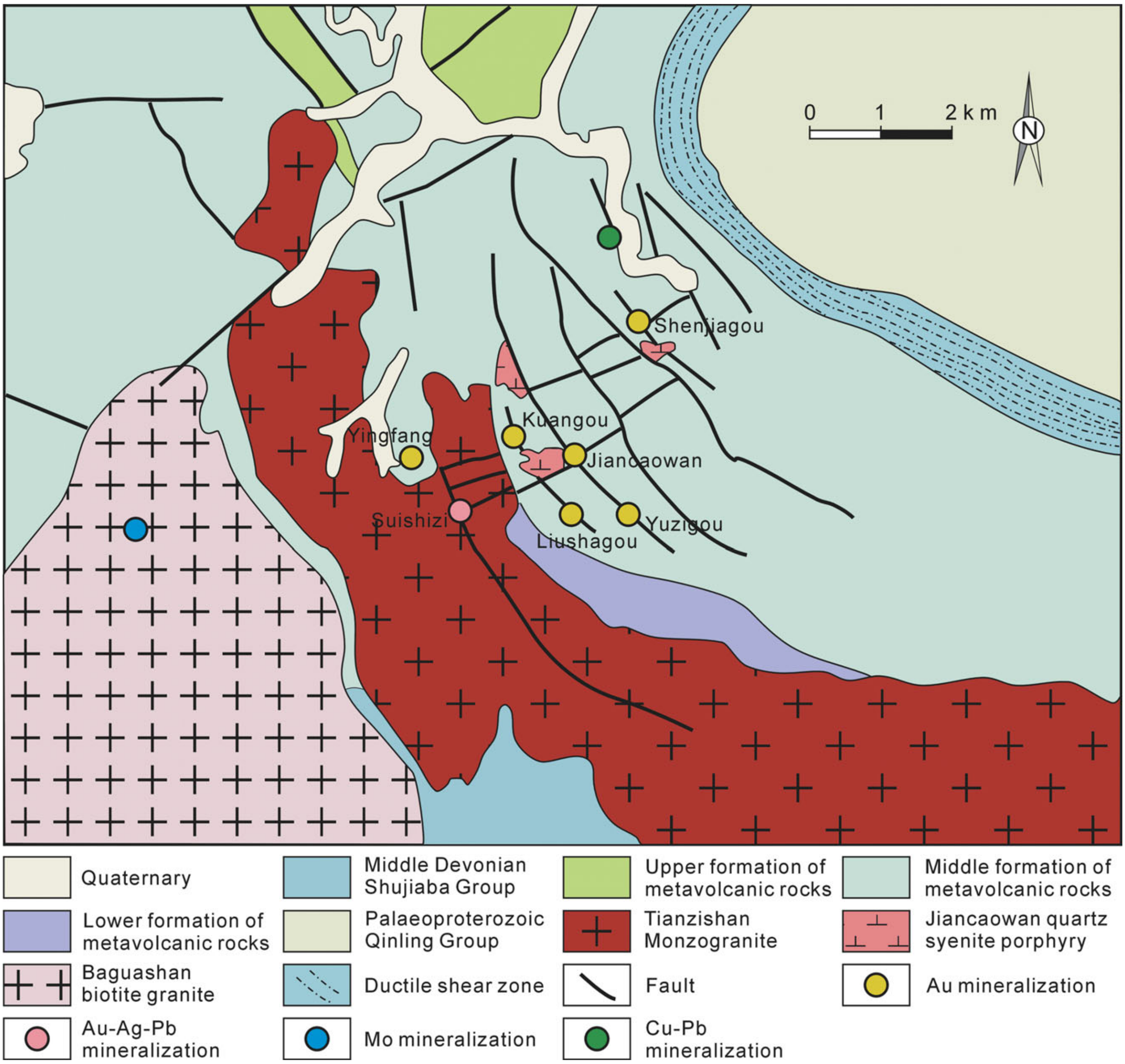

Figure 2. (Colour online) Simplified geological map of the Liziyuan goldfield (modified after Liu *et al.* 2011).

suture is defined by a linear, patchy distribution of arc-related volcanic rocks and ophiolites, which crop out at Yuanyangzhen, Wushan, Guanzizhen, Tangzang, Yanwan, Heihe and Danfeng (Dong *et al.* 2011).

The Mianlue Suture is a younger structure that developed between the South and North China cratons following the northward subduction of the Palaeo-Mianlue Ocean during Late Triassic time between 254 and 220 Ma (Ames, Tilton & Zhou, 1993; Li *et al.* 1996). Ophiolites in the Mianlue Suture include strongly sheared metabasalt, gabbro, ultramafic rocks and radiolarian cherts (Meng & Zhang, 2000; Qin *et al.* 2009; Dong *et al.* 2011). The Late Triassic collisional orogenesis is associated with a widespread granitic magmatism and extensive fold-and-thrust deformation throughout the Qinling Orogen (Zhang *et al.* 2001; Qin *et al.* 2009).

The WQO is bounded by the Linxia–Wushan–Tianshui Fault to the north and the Mianlue Suture to the south (Fig. 1; Zhu *et al.* 2009*a*, 2011). The domain consists of Devonian–Cretaceous sedimentary units. Faults are well developed in the domain and their overall trend is consistent with regional tectonic trends marking the boundaries of major regional lithologies. The faults are structural sites that control the location of regional magmatism where Late Triassic granites are widespread. The granites comprise a ∼ 400 km long granitic belt between the Shangdan and Mianlue sutures, and > 200 plutons crop out in an area totalling ∼ 4000 km^2 (Zhang *et al.* 2009; Zhu *et al.* 2009*a*).

3. Geological features of the goldfield

The Liziyuan goldfield (approximately 34° 12′ 31″ N, 105° 55′ 36″ E) is situated on the northern margin of the WQO and located in Lizi Town, Gansu Province (Fig. 1). The mineralization is part of a cluster of > 30 mineral deposits containing Au, Ag, Cu, Pb, Zn

https://doi.org/10.1017/S0016756812000283 Published online by Cambridge University Press

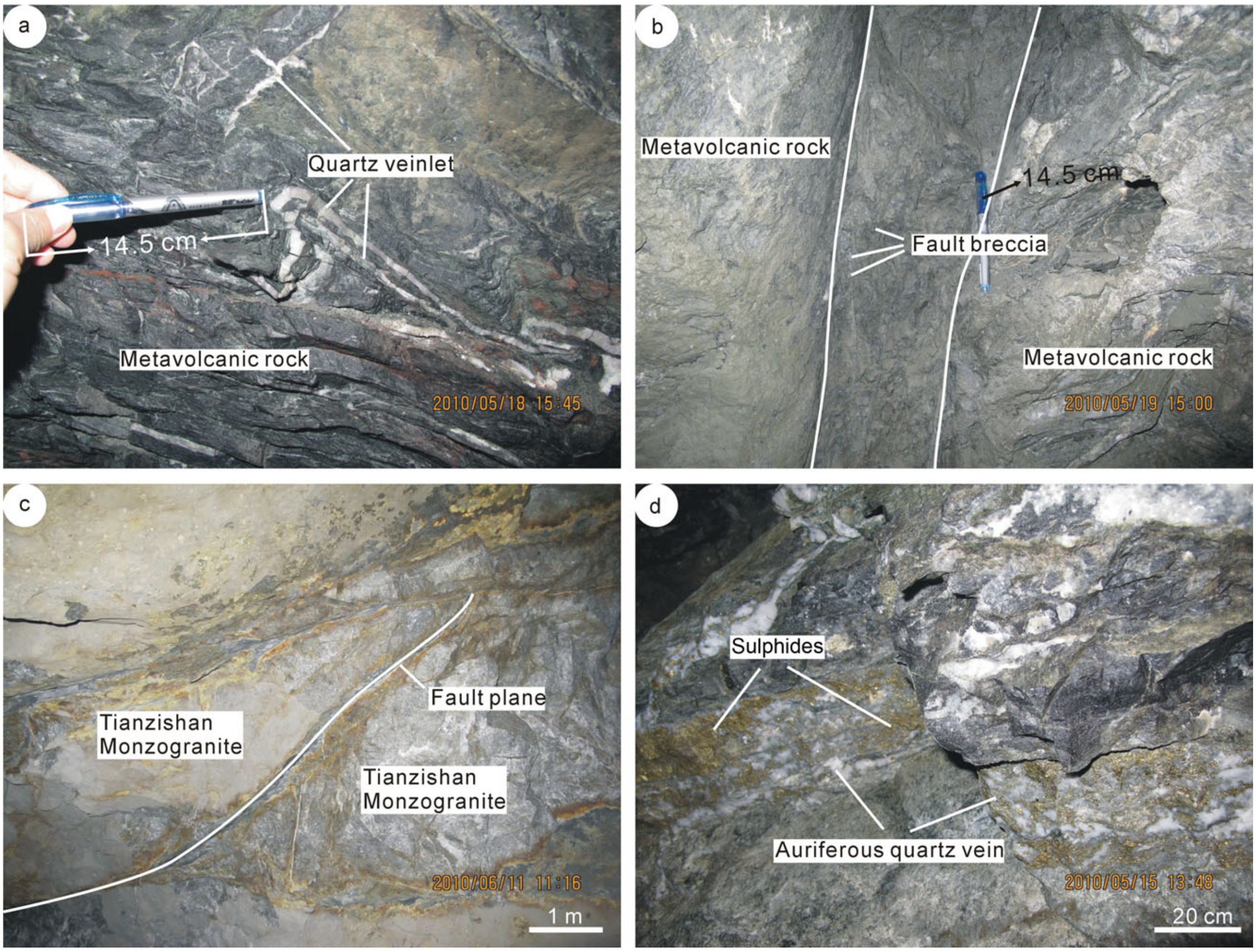

Figure 3. (Colour online) Photographs of tectonic deformation from the Liziyuan goldfield: (a) metamorphic quartz veins with rootless fold structures formed in D_1; (b) ductile-brittle transtensional fault formed in D_2 with straight fault plane and astatic angular-subangular fault breccias; (c) thrust fault in Tianzishan Monzogranite formed in D_3; and (d) NE-striking normal fault formed in D_4 that cuts through auriferous quartz vein.

and Mo (Fig. 2). The goldfield consists of five gold-only deposits, including the Jiancaowan, Kuangou, Yingfang, Liushagou and Yuzigou deposits, which are hosted in metavolcanic rocks, and the Suishizi Au–Ag–Pb polymetallic deposit hosted by the Tianzishan Monzogranite (Fig. 2). The metavolcanic host rocks can be subdivided into three formations (Ding *et al.* 2004; Pei *et al.* 2006). The lower formation is dominated by greenish plagioclase-amphibole schist and biotite-plagioclase-amphibole schist. The overlying formation consists of greenish chlorite-plagioclase-amphibole schist, chlorite schist, chlorite-epidote schist, chlorite-epidote-plagioclase-amphibole schist and minor quartzite. The upper formation consists of light grey ankerite-bearing chlorite-plagioclase-quartz schist and sericite-chlorite-quartz schist, with minor interlayers of quartzite and marble. The orebodies are hosted by the middle and upper formations (Fig. 2).

The unit to the north of the Liziyuan goldfield is the Palaeoproterozoic Qinling Group and the units to the south are metasedimentary units assigned to the Lower Palaeozoic Taiyangsi Formation, Middle Devonian Shujiaba Group, Middle- to Upper Devonian Xihanshui Group and Upper Devonian Dacaotan Group (Fig. 1).

The high degree of shear and compression strain imparted on the regional strata during the Early Silurian to Late Triassic subduction- and accretion-related deformation has disrupted the stratigraphic succession, resulting in discontinuous lenticular compositional domains (Fig. 1).

The formation of mineralization in the Liziyuan goldfield strongly involves a component of structural control. The NW-striking Niangniangba–Shujiaba Fault is a second-order fault that splays off the western part of the Shangdan Suture. The second-order structure has third-order faults that extend through the goldfield. Four phases of deformation (D_1 to D_4) have been recognized in the Liziyuan goldfield. These are: (1) D_1 ductile and dextral NW-striking and SW-dipping (235–260°) steep (65–85°) strike-slip faults, rootless folds, and boudinage and S-C structures (Fig. 3a); (2) D_2 ductile-brittle NW-striking transtensional faults (Fig. 3b); (3) D_3 ductile-brittle thrust faults (that strike 260–285° and dip 45–65°) with compressive-shear structural planes, compressive schistosity, fracture cleavage, drag folding and lesser imbricate fault zones (Fig. 3c); and (4) D_4 normal faults that strike northeast with straight fault

https://doi.org/10.1017/S0016756812000283 Published online by Cambridge University Press

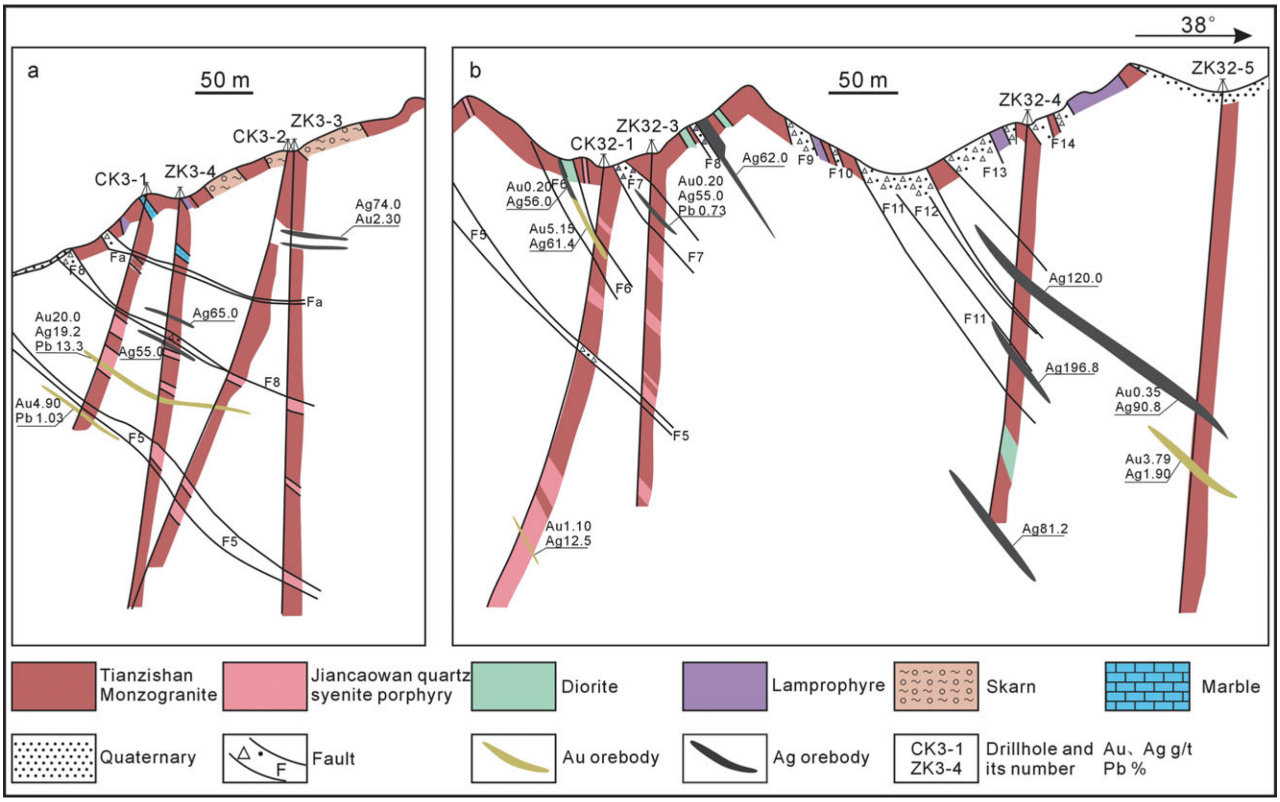

Figure 4. (Colour online) Geological cross-sections of lines 3 (a) and 32 (b) from the Suishizi Au–Ag–Pb polymetallic mineralized site (after Tianshui team of Gansu Bureau of Nonferrous Metal Geology).

planes and astatic angular-subangular fault breccia (Fig. 3d).

Although D_2 is younger than D_1, both deformations may represent a progressive deformation event. The emplacement of the Jiancaowan Porphyry is controlled by these faults. Mineralization is hosted by the D_2 transtensional faults that are disrupted by later D_3 and D_4 structures (Fig. 3d). It is likely the D_2 ore-controlling faults provided vital conduits for the migration of ore-forming fluids, because these structures have 50 to 100 mm wide brown alteration zones with weak limonitization and Au grades between 0.4 and 0.9 g/t, which may be the remnants of ore-forming fluids (Kang & Han, 2003).

The orebodies in the Liziyuan goldfield form diagonal auriferous vein arrays or massive, lenticular and discrete auriferous quartz veins. These auriferous veins are commonly 13 to 265 m in length extending 10 to 260 m down dip, pinch and swell along strike, and are commonly accompanied by disseminated alteration selvages (Fig. 4). Ore in the goldfield has an average grade of 2.58 g/t Au, 12.70 g/t Ag, $<$ 13.3 wt % Pb and $\sim$ 0.15 wt % Cu (Liu & Ai, 2009).

The mineralogy of the auriferous veins is simple including pyrite, chalcopyrite and lesser amounts of galena, freibergite, tetrahedrite and native gold. However, the mineralogy of the Suishizi Au–Ag–Pb deposit is complex, including quartz veining containing about a third in volume of pyrite, galena, chalcopyrite, freibergite, tetrahedrite, zinckenite, argentite, sphalerite and native gold. Apart from quartz, gangue minerals include sericite, carbonate, chlorite, biotite and rutile, and supergene minerals include jarosite, azurite, limonite and malachite. The ore exhibits a subhedral–euhedral granular texture, replacement remnant texture, emulsion texture and cataclastic texture. Massive, veining, veinlet-like and brecciated are the principal structures of the ores. Wall rock alteration includes silication, sericitization, chloritization, epidotization and carbonation. Native gold is common and present in the fractures cutting pyrite and chalcopyrite, and in fractures and vugs in quartz.

Three types of fluid inclusions were recognized in auriferous quartz veins, including the carbonic, mixed CO_2–H_2O and aqueous inclusions that are commonly coexistent (Figs 5, 6). Homogenization temperatures and salinities for the aqueous inclusions range from 173 to 453 °C and 3.4 to 9.1 wt % NaCl equivalent, respectively (Table 1). The final homogenization temperatures for CO_2–H_2O inclusions including both vapour and liquid as homogenized species (Th_{total}) range from 241 to 354 °C (Table 1). The CO_2 homogenization ($T_{h, CO2}$) and clathrate melting temperatures ($T_{m, cla.}$) vary from 23.8 to 29.6 °C and 6.0 to 8.9 °C (Table 1). Salinities of CO_2–H_2O inclusions estimated according to clathrate melting temperatures range from 2.2 to 7.5 wt % NaCl equiv. (Table 1). In general, the Laser Raman spectroscopy analytical results show that CO_2 and H_2O are the main volatiles

https://doi.org/10.1017/S0016756812000283 Published online by Cambridge University Press

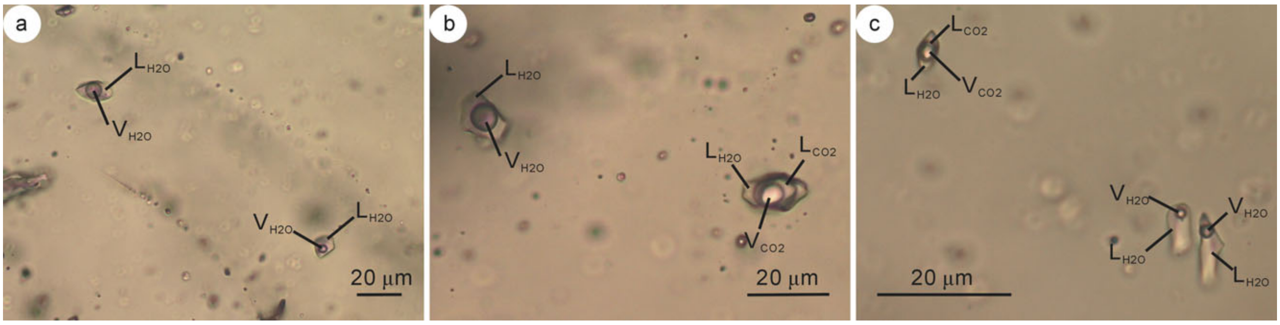

Figure 5. (Colour online) Photomicrographs of fluid inclusion types from gold-bearing quartz veins of the Liziyuan goldfield: (a) isolated two-phase aqueous inclusion; (b) CO_2–H_2O inclusion coexisting with two-phase aqueous inclusions; and (c) coexisting CO_2–H_2O and two-phase aqueous inclusions.

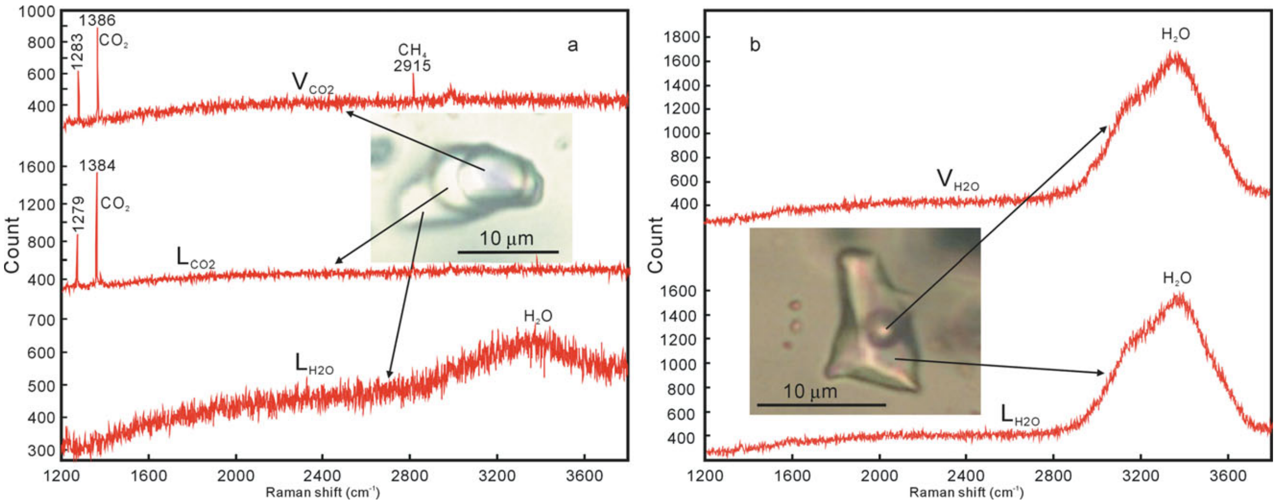

Figure 6. (Colour online) (a) Laser Raman spectra of CO_2–H_2O, and (b) two-phase aqueous inclusions.

in all the measured inclusions, and some bubbles of CO_2–H_2O inclusions contains large quantities of CH_4 (Fig. 6).

4. Petrography of the granitic pluton

Granitic plutons in the Liziyuan goldfield include the Tianzishan Monzogranite to the southwest, the Jiancaowan Porphyry in the central part and many dykes including lamprophyre, diorite and andesite throughout the area (Figs 2, 4). All of the mineralization appears to be spatially associated with the Jiancaowan Porphyry. In this study, we focus on the Tianzishan Monzogranite and Jiancaowan Porphyry, which are described below.

4.a. Tianzishan Monzogranite

The Tianzishan Monzogranite crops out over an area of 250 km^2 and intrudes metavolcanic rocks on its northern margin and Palaeozoic strata on its southern margin. The Palaeozoic units include the Lower Palaeozoic Taiyangsi Formation, Middle Devonian Shujiaba, Middle- to Upper Devonian Xihanshui Group and Upper Devonian Dacaotan Group (Fig. 1). The northern margin of the monzogranite is intensively sheared and folded. The monzogranite is equigranular, generally massive and consists of plagioclase (35 to 40 %), orthoclase (35 to 40 %), quartz (20 to 25 %) and biotite (2 to 4 %), and accessory (2 to 4 %) amounts of apatite, allanite, titanite and zircon. Common microtextures, such as undulose extinction of quartz grains and cataclastic plagioclase phenocrysts rotated along the rupture surface, indicate that the monzogranite has been deformed (Fig. 7a, b). E–W-striking foliation and rotated porphyroclasts indicate metamorphism and deformation are intense in the faults cutting the pluton. The Suishizi Au–Ag–Pb polymetallic deposit is predominantly hosted in the monzogranite with mineralization hosted by cataclastic zones that are hydrothermally altered with sulfide-quartz and pyrite-carbonate forming veinlets in fracture planes in quartz and along fractures in plagioclase grains (Fig. 7a, b).

4.b. Jiancaowan quartz syenite porphyry

The Jiancaowan Porphyry is a quartz syenite covering ~ 200 × 300 m in area that intrudes the middle formation in the metavolcanic rocks described in Section 3 (Fig. 2). The location of the pluton is controlled by the D_2 transtensional faults (Fig. 2). Porphyritic quartz

https://doi.org/10.1017/S0016756812000283 Published online by Cambridge University Press

Table 1. Microthermometric data for fluid inclusions from the Liziyuan goldfield

Sample no.	Ore stage	FI type	Num.	Vapour (vol. %)	T-h (°C)	T-ice (°C)	Tm-CO_2 (°C)	Th-CO_2 (°C)	T-clm (°C)	Salinity (wt % NaCl equiv.)
L-5	II	aqueous	48	10–75	173–361	−5.9 to −2.8				4.7–9.1
		CO_2–H_2O	5	50–85	241–354		−57.2 to −56.8	27.4–28.2	8.0–8.9	2.2–4.0
L-6	II	aqueous	35	10–80	180–453	−5.5 to −2.0				3.4–8.6
		CO_2–H_2O	4	35–80	278–317		−56.9 to −56.7	23.8–29.6	6.0–8.0	4.0–7.5
1558–2	II	aqueous	27	10–50	182–395	−5.3 to −2.9				4.3–8.3

Three samples of quartz from stage II were prepared as 100 µm thick doubly polished sections for fluid inclusion studies. Microthermometric measurements were conducted using a Linkam MDS600 heating–freezing stage at the State Key Laboratory of Geological Processes and Mineral Resources, China University of Geosciences, Wuhan. The heating–freezing rate is generally 0.2–5 °C min^{-1}, but reduced to less than 0.2 °C min^{-1} near the phase transformation. The heating–freezing stage was calibrated using the synthetic fluid inclusion standard produced by Fluid Inc. The estimated temperature errors were ± 0.1 °C at temperatures below 30 °C and ± 1 °C at temperatures above 30 °C. Salinities of the two-phase aqueous and CO_2–H_2O inclusions were calculated using the equation of $W = 0.00 + 1.78T_{ice} - 0.0442T_{ice}^2 + 0.000557T_{ice}^3$ (Bodnar, 1993) and $W = 15.52022 - 1.02342\ T_{clm} - 0.05286\ T_{clm}^2$ (Roedder, 1984), respectively.
Compositions of single fluid inclusions were analysed using a Renishaw MK1–1000 Laser Raman probe, also at the State Key Laboratory of Geological Processes and Mineral Resources, China University of Geosciences, Wuhan. The wavelength of Ar^+ laser is 514.5 nm and the measured spectrum time is 30 s. Laser power is of 2 to 4 mw for a micrometre size and the size of laser beam spot is 2 µm. The spectrum diagram is taken from the wave band of 1200 to 3800 cm^{-1}.
T-h – final homogenization temperature of fluid inclusion; T-ice – final melting temperature of ice; Tm-CO_2 – final melting temperature of solid CO_2; Th-CO_2 – homogenization temperature of CO_2; T-clm – dissolution temperature of CO_2.

syenite dykes also intrude transtensional faults in the Tianzishan Monzogranite and the metavolcanic rocks, providing a possible time relationship between the monzogranite and porphyry (Fig. 4). The Jiancaowan Porphyry is porphyritic with phenocrysts of orthoclase, quartz, biotite and amphibole in a matrix consisting of plagioclase laths and minor anhedral granular quartz, and accessory pyrite, apatite and zircon. Orthoclase phenocrysts have a subhedral–euhedral granular texture with carlsbad twinning and are commonly replaced by epidote (Fig. 7c). Quartz phenocrysts are embayed due to the partial melting of the phenocrysts. The biotite and amphibole are commonly altered to chlorite and epidote, and the plagioclase in the matrix is sericitized. Although the porphyry has minor amounts of pyrite, a few orebodies have been discovered in the pluton (Fig. 4).

5. Sampling and analytical methods

5.a. Major and trace element analyses

Least altered samples from the Tianzishan Monzogranite and Jiancaowan Porphyry were collected for whole-rock major and trace element analyses completed at the State Key Laboratory of Continental Dynamics of Northwest University in Xi'an, China. The samples were powdered to a 200 mesh size using a tungsten carbide ball mill. Major elements were analysed by X-ray fluorescence (XRF) (Rikagu RIX2100), using the BCR-2 and GBW07105 standards at an accuracy of ± 5 %. For trace element analysis, sample powders were digested using an HF+HNO_3 mixture in high-pressure Teflon bombs at 190 °C for 48 hours. Trace elements were analysed using an inductively coupled plasma mass spectrometer (ICP-MS) (Agilent 7500a) produced by Perkin Elmer/SCICX, with Rh and BHVO-1 as reference materials, and the analytical precision was generally better that ± 10 %.

5.b. LA-ICP-MS U–Pb dating and Hf isotopic analytical methods

Two samples (TZS-6 and TZS-7) from the Tianzishan Monzogranite and one (JCW-1) from the Jiancaowan Porphyry were chosen for *in situ* zircon U–Pb dating and Lu–Hf isotopic analyses. Zircons were extracted from the three samples using heavy liquid and magnetic separation methods. The zircons were then mounted in epoxy resin and polished until their interiors were exposed, cleaned and gold-coated for maximum surface conductivity. The interior morphology of the zircons was revealed using cathodoluminescence (CL) images before U–Pb dating using a Neptune multi-collector ICP-MS (MC-ICP-MS) equipped with a 193 nm Excimer laser at the State Key Laboratory of Continental Dynamics of Northwest University in Xi'an, China. The analyses adopted a laser spot size of 30 µm for ablation (Yuan *et al.* 2004). During the dating, the Harvard zircon 91500 was used as an

https://doi.org/10.1017/S0016756812000283 Published online by Cambridge University Press

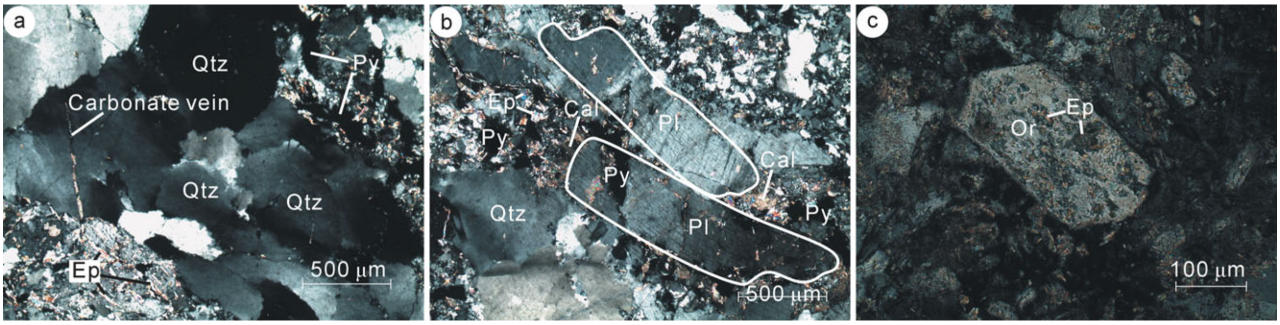

Figure 7. (Colour online) Microphotographs of the Tianzishan Monzogranite and Jiancaowan Porphyry. All microphotographs were taken under polarized light. (a) Tianzishan Monzogranite: quartz with undulose extinction texture and hydrothermal pyrite-carbonate veinlets metasomatized and filled along fracture planes in quartz. (b) Tianzishan Monzogranite: cataclastic plagioclase phenocryst rotated and slipped along the rupture surface; hydrothermal sulphide-quartz and pyrite-carbonate veinlets metasomatized and filled along fractures in plagioclase grains. (c) The Jiancaowan Porphyry has a porphyritic texture; the subhedral-euhedral orthoclase phenocryst was replaced by epidote. Qtz – quartz; Cal – calcite; Pl – plagioclase; Py – pyrite; Ep – epidote; Or – orthoclase.

external standard to calibrate instrumental bias and isotopic fractionation, ^{29}Si was used as the internal calibrant, and the NIST 610 standard for calibrating U, Th and Pb concentrations in zircons with unknown dates. Although common Pb has a minimal effect on the age results, corrections for common Pb were made using the method of Andersen (2002). The age calculations and plotting of concordia diagrams were made using the Isoplot (ver. 3.0) program of Ludwig (2003). Errors for individual analyses are quoted at the 1σ level; weighted mean ages were calculated at the 2σ level.

In situ zircon Lu–Hf isotopic analyses were also conducted using a Neptune MC-ICP-MS equipped with a 193 nm laser, at the State Key Laboratory of Continental Dynamics. During the analyses, a laser repetition rate of 10 Hz at 100 mJ was used for ablation and laser spot sizes were 44 μm. Interference between ^{176}Lu and ^{176}Hf was eliminated by measuring the intensity of the interference-free ^{175}Lu. The recommended $^{176}Lu/^{175}Lu$ ratio of 0.02669 (DeBievre & Taylor, 1993) was used to calculate $^{176}Lu/^{177}Hf$. Similarly, the isobaric interference of ^{176}Yb on ^{176}Hf was corrected by using a recommended $^{176}Yb/^{172}Yb$ ratio of 0.5886 (Chu *et al.* 2002) to calculate $^{176}Hf/^{177}Hf$ ratios. Zircon 91500 was used as the reference material for calibration and controlling the condition of the analytical instrumentation (Yuan *et al.* 2008). During analyses, the $^{176}Hf/^{177}Hf$ ratios of 91500 and GJ-1 were 0.282307 ± 4 (2σ, n = 30) and 0.282015 ± 2 (2σ, n = 30), respectively, which is compatible with the recommended $^{176}Hf/^{177}Hf$ ratios of 0.2823075 ± 58 (2σ) for 91500 and 0.282015 ± 19 (2σ) for GJ-1 (Wu *et al.* 2006; Elhlou *et al.* 2006).

We have adopted a decay constant of 1.867×10^{-11} yr^{-1} for ^{176}Lu (Sŏderlund *et al.* 2004). Initial $^{176}Hf/^{177}Hf$ ratio ($\varepsilon_{Hf}(t)$) is calculated relative to the chondritic reservoir with a $^{176}Hf/^{177}Hf$ ratio of 0.282772 and $^{176}Lu/^{177}Hf$ of 0.0332 (Blichert-Toft & Albarède, 1997). Single-stage Hf model ages (T_{DM1}) are calculated relative to the depleted mantle with a present-day $^{176}Hf/^{177}Hf$ ratio of 0.28325 and $^{176}Lu/^{177}Hf$ of 0.0384, and two-stage Hf model ages (T_{DM2}) are calculated by assuming a mean $^{176}Lu/^{177}Hf$ value of 0.0093 for the average upper continental crust (Vervoort & Patchett, 1996; Vervoort & Blichert-Toft, 1999).

6. Analytical results

6.a. Major and trace elements

Major and trace element compositions of the Tianzishan Monzogranite samples are listed in Table 2. The monzogranite has a wide range in chemical composition and most of the samples have higher K_2O contents (between 4.33 and 6.84 wt % with an average of 5.39 %) than Na_2O (between 2.14 and 4.24 wt % with an average of 3.05 wt %). The exception is Sample TZS-1 with Na_2O = 7.56 wt %, K_2O = 1.46 wt % and Na_2O/K_2O = 5.18. The Shands Index A/CNK ($Al_2O_3/(CaO + K_2O + Na_2O)$) values vary from 0.66 to 1.22 and indicate that the monzogranite is metaluminous to peraluminous (Fig. 8b). On a SiO_2–K_2O diagram, the monzogranite plots in the upper right corner of the high-K (calc-alkaline) field (Fig. 8a).

The monzogranite has an enriched light rare earth element (LREE) and depleted heavy rare earth element (HREE) chondrite-normalized pattern (Fig. 9a), with $(La/Yb)_N$ between 5.48 and 53.4 (with an average of 24.4) and $(Gd/Yb)_N$ between 1.39 and 3.57 (with an average of 2.40). The monzogranite can be distinctly subdivided into two phases, one with positive Eu anomalies (Eu/Eu* = 1.04–1.65) and the other with negative Eu anomalies (Eu/Eu* = 0.58–0.89). Using primitive mantle-normalized spider diagrams, all samples show spikes in Rb, Th, U, K and troughs in Nb, Ta, Ti (Fig. 9b). The samples of the first phase are depleted in Ba and Sr, whereas the other phase is enriched in these elements (Fig. 9b).

Assays for the Jiancaowan Porphyry are listed in Table 2. Compared with normal crustal-derived felsic magmas, all samples of the Jiancaowan Porphyry have relatively higher contents of MgO between 0.85 and

https://doi.org/10.1017/S0016756812000283 Published online by Cambridge University Press

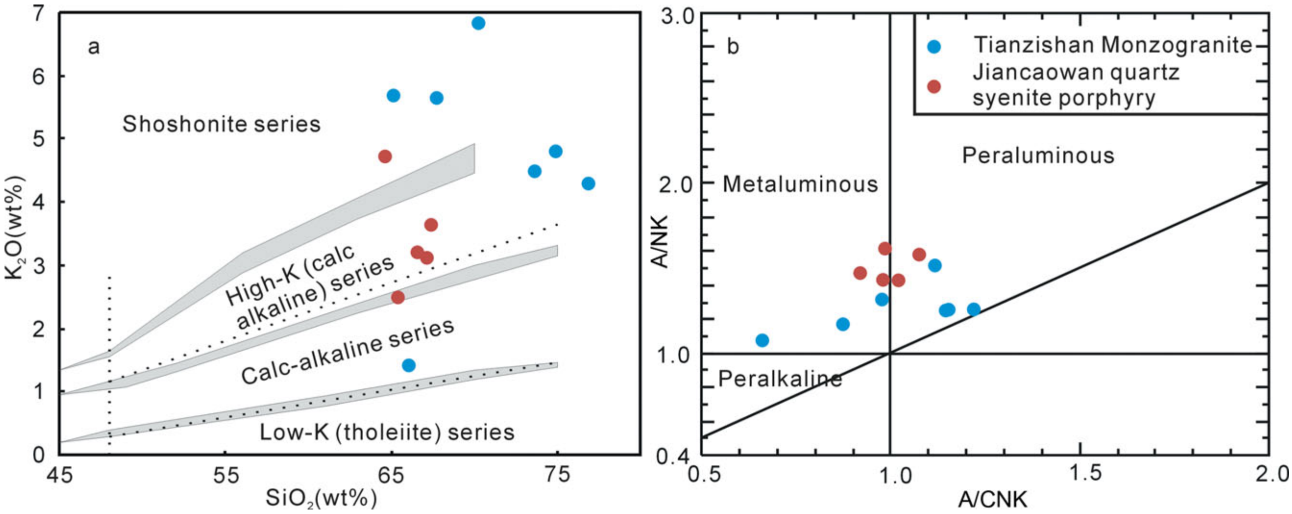

Figure 8. (Colour online) SiO_2 versus K_2O (a) and A/CNK versus A/NK (b) plots for the Tianzishan Monzogranite and Jiancaowan Porphyry. A/CNK – molar ratio of $Al_2O_3/(CaO + Na_2O + K_2O)$; A/NK – molar ratio of $Al_2O_3/(Na_2O + K_2O)$.

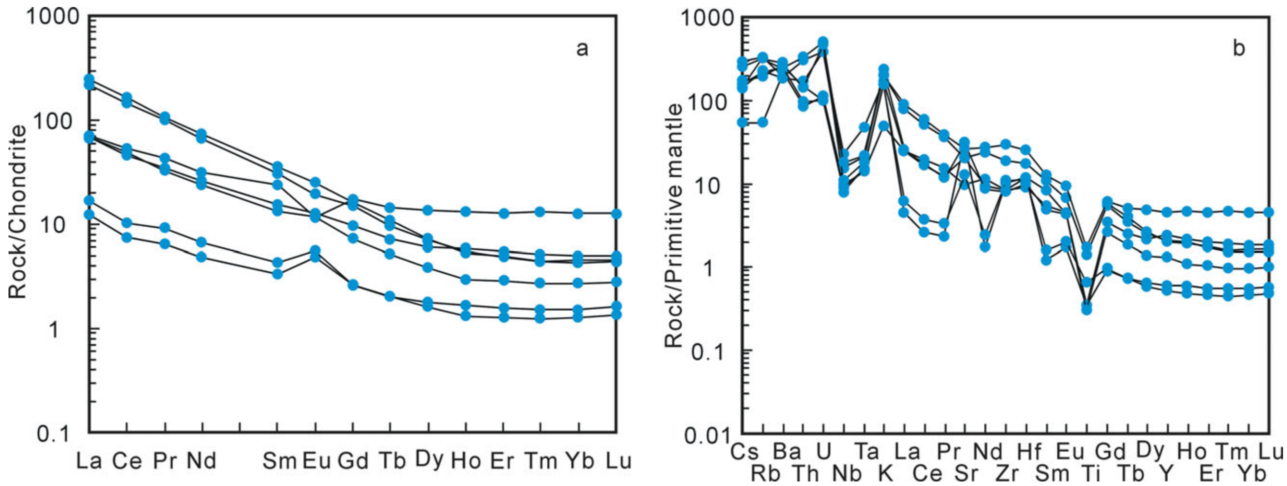

Figure 9. (Colour online) (a) Chondrite-normalized REE patterns, and (b) and primitive mantle-normalized trace element patterns for the Tianzishan Monzogranite. Chondrite and primitive mantle data after McDonough & Sun (1995).

2.08 wt % with Mg no. (Mg no. = Mg/(Mg + Fe) × 100) ranging from 43.4 to 58.2. The Jiancaowan Porphyry also has relatively higher Na_2O contents of 2.57–4.12 wt %, K_2O contents of 2.59–4.89 wt % and Na_2O/K_2O ratios of 0.53–1.59 (with an average of 1.10). The A/CNK is 0.92–1.08 with an average of 1.00, which indicates that these rocks are metaluminous to weakly peraluminous (Fig. 8b). On a SiO_2 versus K_2O diagram, most of the samples plot within the high-K (calc-alkaline) field (Fig. 8a).

The quartz syenite porphyry samples have $(La/Yb)_N$ ratios of 14.1–18.0 (with an average of 15.7), $(Gd/Yb)_N$ ratios of 1.82–2.56 (with an average of 2.05) and weakly negative Eu anomalies ($Eu/Eu^* = 0.85$–0.91). Chondrite-normalized REE patterns show that all samples are enriched in LREEs and depleted in HREEs (Fig. 10a). On the primitive mantle-normalized spider diagrams (Fig. 10b), the samples have spikes in Rb, Ba, U, K and Sr, and troughs in Nb, Ta and Ti. Their Nb/Ta ratios (11.7–13.4, with an average of 12.4) are compatible with the upper crust (∼ 12, Taylor & Mclennan, 1995). They have Rb and Sr contents of 102–163 ppm and 258–781 ppm, respectively, with Rb/Sr ratios of 0.21–0.47. Compared with normal crustal-derived felsic magmas, they have a relatively high abundance of Cr (20.1–53.2 ppm) and Ni (10.1–33.1 ppm), with Cr/Ni ratios of 1.61–2.01.

6.b. LA-ICP-MS U–Pb ages

Zircon CL images and U–Pb isotopic results of TZS-6 and TZS-7 sampled from the Tianzishan Monzogranite are presented in Figure 11 and the isotope data are listed in Table 3. Zircons from TZS-6 are euhedral crystals exhibiting oscillatory zoning and range from 100 to 150 μm in size. For TZS-6, a total of 13 analyses were carried out on 13 zircons. They have U contents of 536–2819 ppm and Th contents of 260–1510 ppm with Th/U ratios of 0.36–0.73, suggesting a magmatic origin. The ^{206}Pb–^{238}U ages vary from 250 ± 3 to 264 ± 3 Ma and have a weighted mean age of 260.0 ± 2.1 Ma (MSWD = 1.3, 2σ). Zircons from

https://doi.org/10.1017/S0016756812000283 Published online by Cambridge University Press

Table 2. Major and trace element analyses of the Tianzishan Monzogranite and Jiancaowan Porphyry

	Tianzishan monzogranite							Jiancaowan quartz syenite porphyry				
Sample no.	TZS-1	TZS-2	TZS-4	TZS-6	TZS-7	SSZ-2	SSZ-9	JCW-1	JCW-2	JCW-3	JCW-4	JCW-9
Major oxides (wt %)												
SiO_2	66.05	73.67	74.88	67.74	77.79	65.09	70.19	67.15	66.55	67.37	65.39	64.62
TiO_2	0.07	0.07	0.00	0.28	0.13	0.34	0.06	0.32	0.33	0.33	0.44	0.44
Al_2O_3	15.11	15.08	13.55	15.26	12.03	15.57	12.81	14.64	14.48	14.78	15.22	15.45
TFe_2O_3	0.86	0.56	1.13	1.53	0.81	2.10	0.80	2.55	2.52	2.27	3.48	2.58
MnO	0.06	0.00	0.02	0.05	< 0.01	0.07	0.08	0.05	0.06	0.05	0.05	0.10
MgO	0.15	0.18	0.24	1.00	0.35	0.67	1.16	1.37	1.35	1.29	2.08	0.85
CaO	4.81	0.59	0.58	1.94	0.17	2.25	2.03	2.57	3.25	2.30	2.50	3.36
Na_2O	7.56	4.24	3.26	2.30	2.95	3.43	2.14	4.08	3.77	3.76	4.12	2.57
K_2O	1.46	4.64	4.97	5.85	4.33	5.69	6.84	3.24	3.34	3.78	2.59	4.89
P_2O_5	0.04	0.04	0.02	0.11	0.02	0.17	0.03	0.10	0.11	0.11	0.13	0.15
LOI	4.19	1.23	1.62	3.93	0.87	3.72	3.39	4.24	4.50	4.00	4.03	5.08
TOTAL	100.36	100.30	100.27	99.99	99.45	99.10	99.53	100.31	100.26	100.04	100.03	100.09
Na_2O+K_2O	9.02	8.88	8.23	8.15	7.28	9.12	8.98	7.32	7.11	7.54	6.71	7.46
Na_2O/K_2O	5.18	0.91	0.66	0.39	0.68	0.60	0.31	1.26	1.13	0.99	1.59	0.53
Mg no.	28.9	42.8	33.1	60.4	50.2	42.6	77.2	55.6	55.5	57.0	58.2	43.4
σ	3.53	2.57	2.12	2.68	1.52	3.77	2.97	2.22	2.15	2.33	2.01	2.57
A/CNK	0.66	1.15	1.15	1.12	1.22	0.98	0.87	0.98	0.92	1.02	1.08	0.99
A/NK	1.08	1.26	1.26	1.51	1.26	1.32	1.17	1.43	1.47	1.44	1.59	1.62
Trace elements (ppm)												
Li	10.8	6.82	5.21	10.7	19.7	3.90	6.22	14.5	18.5	17.6	20.1	11.9
Be	2.03	3.41	2.44	3.50	2.15	2.47	1.75	2.18	2.13	2.16	2.26	2.60
Sc	2.83	1.62	1.86	2.73	1.84	3.61	1.29	5.63	5.58	5.51	7.70	6.01
V	7.75	5.66	0.75	18.8	19.9	32.0	5.83	41.0	41.2	41.9	58.8	52.7
Cr	1.04	1.95	0.66	16.5	16.8	26.8	3.23	31.4	35.7	32.1	53.2	20.1
Co	33.6	110	80.7	87.3	121	75.7	91.2	55.3	58.4	53.9	42.7	44.1
Ni	3.14	1.27	0.37	7.92	8.08	16.8	8.76	16.6	17.8	18.0	33.1	10.1
Cu	1.52	1.58	17.3	5.15	2.43	113	5.09	2.63	6.46	12.4	17.1	33.8
Zn	19.1	33.0	17.5	20.5	14.2	2310	18.7	41.1	27.4	21.8	39.8	27.1
Ga	19.0	20.0	14.6	20.4	15.9	17.7	15.8	17.1	17.1	17.4	18.3	18.6
Ge	0.88	0.84	1.29	1.54	0.86	1.47	0.93	1.30	1.29	1.23	1.07	1.61
Rb	32.9	130	138	198	114	193	189	109	113	129	102	163
Sr	405	631	196	407	253	517	600	303	313	275	258	781
Y	10.3	2.57	19.6	8.80	2.23	8.55	5.70	11.4	11.6	10.8	12.4	10.3
Zr	86.3	108	87.8	195	112	302	82.8	131	125	134	155	139
Nb	6.45	5.13	15.0	10.0	5.88	11.8	7.06	13.3	13.4	13.4	15.4	15.0
Cs	1.16	3.26	2.93	6.03	3.57	2.94	5.33	4.77	4.29	4.43	4.57	2.52
Ba	1465	1632	1249	1282	1718	1604	1863	1001	1061	910	455	1198
La	16.0	2.87	16.2	50.8	3.92	57.4	16.4	24.1	23.3	22.0	27.4	22.4
Ce	27.8	4.46	32.4	88.2	6.29	98.1	29.1	43.9	42.5	39.9	50.2	42.1
Pr	3.20	0.59	3.86	9.07	0.85	9.77	2.96	4.73	4.66	4.30	5.39	4.71
Nd	11.6	2.15	14.2	30.0	3.05	33.5	10.7	16.9	16.5	15.5	19.2	17.5
Sm	2.20	0.49	3.40	4.52	0.63	5.15	1.93	3.02	2.99	2.78	3.37	3.25
Eu	0.69	0.26	0.65	1.06	0.31	1.41	0.66	0.77	0.78	0.74	0.89	0.88
Gd	1.87	0.50	3.45	2.93	0.52	3.22	1.41	2.55	2.57	2.38	2.83	2.68
Tb	0.25	0.074	0.51	0.35	0.072	0.39	0.19	0.34	0.35	0.32	0.38	0.36
Dy	1.46	0.44	3.21	1.69	0.39	1.78	0.93	2.00	2.01	1.88	2.21	1.94
Ho	0.31	0.091	0.70	0.30	0.071	0.28	0.16	0.41	0.42	0.40	0.45	0.37
Er	0.87	0.25	1.98	0.77	0.21	0.78	0.45	1.11	1.10	1.07	1.17	0.97
Tm	0.13	0.038	0.31	0.11	0.031	0.11	0.066	0.16	0.17	0.16	0.17	0.14
Yb	0.79	0.24	2.01	0.68	0.20	0.73	0.43	1.09	1.10	1.06	1.11	0.85
Lu	0.12	0.039	0.30	0.11	0.033	0.11	0.067	0.17	0.17	0.17	0.17	0.13
Hf	2.55	3.38	3.37	4.83	3.20	7.23	2.83	3.59	3.43	3.62	3.92	3.56
Ta	0.53	0.56	1.77	0.80	0.55	0.80	0.65	1.14	1.12	1.13	1.17	1.12
Pb	30.1	41.6	16.1	358	13.9	1208	76.3	20.2	16.2	10.5	14.6	53.4
Th	6.72	11.5	13.9	24.5	7.69	26.4	11.3	10.1	9.85	9.74	9.94	7.51
U	2.35	2.04	7.96	8.01	1.99	10.2	9.53	3.59	3.18	3.67	3.23	2.88
Eu/Eu*	1.04	1.60	0.58	0.89	1.65	1.05	1.21	0.85	0.86	0.88	0.87	0.91
ΣREE	67.2	12.5	83.2	191	16.6	213	65.5	101	98.7	92.7	115	98.2
LREE/HREE	10.6	6.49	5.67	26.5	9.85	27.7	16.7	11.9	11.5	11.5	12.5	12.2
$(La/Yb)_N$	13.8	8.12	5.48	50.8	13.0	53.4	26.0	15.0	14.5	14.1	16.8	18.0
$(Gd/Yb)_N$	1.92	1.69	1.39	3.49	2.05	3.57	2.66	1.90	1.90	1.82	2.07	2.56

Mg no. = (molecular MgO/(MgO + Fe_2O_3) × 100); A/CNK = (molecular Al_2O_3/(CaO + Na_2O + K_2O)); A/NK = (molecular Al_2O_3/(Na_2O + K_2O)); $\sigma = ((SiO_2 - 43)/(Na_2O + K_2O))$; Eu/Eu* = $((Sm)_N \times (Gd)_N)^{1/2}$; Chondrite data after McDonough & Sun (1995).

TZS-7 are mostly between 80 and 150 μm in size and have regular oscillatory magmatic zoning. They have variable U contents of 421–2398 ppm, Th contents of 56.0–806 ppm and Th/U ratios of 0.06–0.83. Ten U–Pb analyses plot in a group on the concordia curve giving a weighted mean ^{206}Pb–^{238}U age of 256.1 ± 3.7 Ma (MSWD = 0.53, 2σ). Therefore, the U–Pb ages of 256.1 ± 3.7 to 260.0 ± 2.1 Ma should be the best estimates for the crystallization age of the Tianzishan Monzogranite.

https://doi.org/10.1017/S0016756812000283 Published online by Cambridge University Press

Table 3. LA-ICP-MS zircon U–Pb data for the Tianzishan Monzogranite and Jiancaowan Porphyry

	Concentrations (ppm)				Isotopic ratios						Calculated ages (Ma)					
Spot no.	Pb	Th	U	Th/U	$^{207}Pb/^{206}Pb$	1σ	$^{207}Pb/^{235}U$	1σ	$^{206}Pb/^{238}U$	1σ	$^{207}Pb–^{206}Pb$	1σ	$^{207}Pb–^{235}U$	1σ	$^{206}Pb–^{238}U$	1σ
TZS-6 from the Tianzishan Monzogranite																
1	196	477	933	0.51	0.05150	0.00164	0.29735	0.00911	0.04187	0.00048	263	49	264	7	264	3
4	539	1510	2819	0.53	0.05197	0.00137	0.29650	0.00747	0.04137	0.00045	284	38	264	6	261	3
5	353	1105	1815	0.61	0.05372	0.00149	0.29334	0.00780	0.03960	0.00044	359	40	261	6	250	3
7	106	260	536	0.49	0.05165	0.00236	0.29451	0.01305	0.04134	0.00057	270	76	262	10	261	4
8	118	336	582	0.58	0.05138	0.00231	0.29452	0.01288	0.04157	0.00057	258	75	262	10	263	4
10	260	897	1224	0.73	0.05404	0.00157	0.30601	0.00854	0.04106	0.00047	373	42	271	7	259	3
15	407	806	2097	0.38	0.05163	0.00157	0.29541	0.00863	0.04149	0.00048	269	46	263	7	262	3
22	241	471	1280	0.37	0.05084	0.00180	0.28849	0.00985	0.04115	0.00052	234	55	257	8	260	3
23	344	728	1786	0.41	0.05099	0.00175	0.29046	0.00964	0.04131	0.00052	240	53	259	8	261	3
27	330	1159	1906	0.61	0.05441	0.00201	0.31024	0.01110	0.04134	0.00054	388	57	274	9	261	3
29	170	605	844	0.71	0.05159	0.00205	0.29161	0.01122	0.04099	0.00056	267	63	260	9	259	3
32	427	1117	2260	0.50	0.05553	0.00194	0.31368	0.01060	0.04097	0.00053	434	52	277	8	259	3
33	245	469	1295	0.36	0.05192	0.00195	0.29644	0.01075	0.04140	0.00056	282	58	264	8	262	3
TZS-7 from the Tianzishan Monzogranite																
1	234	205	1262	0.16	0.05128	0.00163	0.29090	0.00778	0.04113	0.00102	253	27	259	6	260	6
5	109	214	592	0.36	0.05149	0.00183	0.29236	0.00901	0.04117	0.00103	263	32	260	7	260	6
13	103	366	533	0.69	0.05350	0.00196	0.29186	0.00935	0.03956	0.00100	350	33	260	7	250	6
19	93.2	110	507	0.22	0.05530	0.00207	0.30343	0.01001	0.03979	0.00101	424	34	269	8	252	6
20	446	806	2398	0.34	0.05392	0.00176	0.29889	0.00829	0.04020	0.00100	368	28	266	6	254	6
23	305	396	1685	0.24	0.05587	0.00183	0.30806	0.00857	0.03998	0.00100	447	28	273	7	253	6
25	89.5	351	421	0.83	0.05531	0.00198	0.30557	0.00958	0.04006	0.00101	425	32	271	7	253	6
26	155	468	797	0.59	0.05246	0.00178	0.29344	0.00860	0.04056	0.00102	306	30	261	7	256	6
27	177	56	934	0.06	0.05315	0.00180	0.30496	0.00889	0.04160	0.00105	335	30	270	7	263	6
34	95.2	344	502	0.69	0.05038	0.00181	0.28579	0.00896	0.04113	0.00104	213	33	255	7	260	6
JCW-1 from the Jiancaowan Porphyry																
2	147	363	827	0.44	0.05038	0.00214	0.25131	0.01040	0.03616	0.00049	213	71	228	8	229	3
3	106	237	504	0.47	0.05341	0.00186	0.26885	0.00913	0.03649	0.00046	346	54	242	7	231	3
4	71.1	221	351	0.63	0.05190	0.00225	0.25540	0.01078	0.03567	0.00049	281	71	231	9	226	3
5	335	641	2076	0.31	0.05338	0.00158	0.26584	0.00768	0.03610	0.00043	345	44	239	6	229	3
6	124	406	713	0.57	0.05047	0.00291	0.25497	0.01432	0.03663	0.00059	217	100	231	12	232	4
8	69.7	111	331	0.34	0.05118	0.00169	0.25416	0.00816	0.03601	0.00044	249	51	230	7	228	3
9	113	618	592	1.04	0.05139	0.00253	0.25726	0.01232	0.03630	0.00054	258	83	232	10	230	3
13	60.2	52.7	303	0.17	0.05313	0.00192	0.26571	0.00929	0.03627	0.00046	334	56	239	7	230	3
15	158	365	825	0.44	0.05276	0.00177	0.26615	0.00864	0.03659	0.00045	318	51	240	7	232	3
16	103	250	497	0.50	0.05145	0.00219	0.25745	0.01063	0.03630	0.00050	261	69	233	9	230	3
18	99.4	196	553	0.35	0.04933	0.00160	0.24676	0.00772	0.03629	0.00044	164	50	224	6	230	3
19	115	393	627	0.63	0.05083	0.00178	0.25232	0.00857	0.03601	0.00045	233	55	228	7	228	3
20	125	281	636	0.44	0.05042	0.00157	0.25032	0.00751	0.03602	0.00043	214	47	227	6	228	3
22	100	614	431	1.43	0.05072	0.00186	0.25053	0.00885	0.03583	0.00046	228	58	227	7	227	3
24	176	577	1000	0.58	0.05075	0.00174	0.25284	0.00831	0.03614	0.00045	229	53	229	7	229	3
29	153	583	744	0.78	0.05341	0.00186	0.26775	0.00894	0.03637	0.00046	346	53	241	7	230	3
32	161	563	763	0.74	0.05102	0.00184	0.25209	0.00867	0.03584	0.00046	242	55	228	7	227	3
33	86.0	257	410	0.63	0.05105	0.00246	0.25491	0.01186	0.03622	0.00054	243	80	231	10	229	3
39	20.7	32.5	55.0	0.59	0.04972	0.00210	0.24780	0.00999	0.03615	0.00050	182	68	225	8	229	3
41	99.7	565	493	1.15	0.05095	0.00235	0.25580	0.01126	0.03640	0.00054	239	74	231	9	230	3
42	106	424	536	0.79	0.05109	0.00220	0.25424	0.01039	0.03608	0.00052	245	67	230	8	228	3
43	165	615	853	0.72	0.05131	0.00217	0.25959	0.01040	0.03667	0.00052	255	66	234	8	232	3
44	135	373	736	0.51	0.05007	0.00228	0.25006	0.01084	0.03620	0.00053	198	73	227	9	229	3
10	60.0	85.6	138	0.62	0.06636	0.00291	1.20673	0.01432	0.13188	0.00059	818	17	804	7	799	3
11	51.7	53.5	74.9	0.71	0.06475	0.00303	1.12787	0.05123	0.12634	0.00196	766	69	767	24	767	11
21	276	176	530	0.33	0.06392	0.00203	1.05149	0.03214	0.11934	0.00148	739	44	730	16	727	9
34	333	5.68	239	0.02	0.10427	0.00342	4.33339	0.13466	0.30145	0.00397	1701	38	1700	26	1698	20
35	240	234	373	0.63	0.06571	0.00218	1.18990	0.03736	0.13134	0.00167	797	44	796	17	796	10
38	182	95.4	96.0	0.99	0.11420	0.00392	5.23461	0.16953	0.33242	0.00453	1867	39	1858	28	1850	22

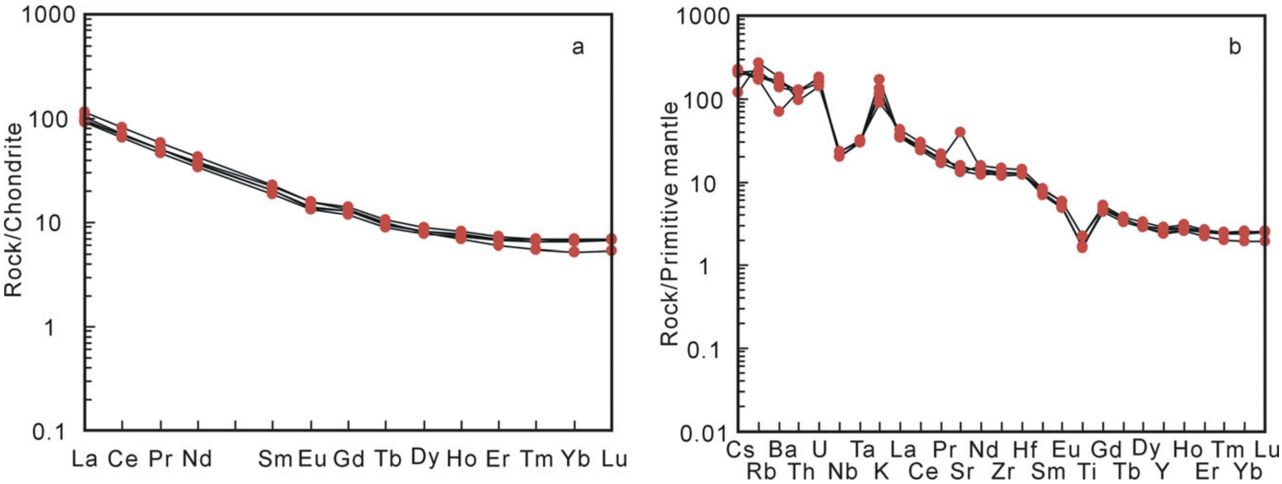

Figure 10. (Colour online) (a) Chondrite-normalized REE patterns, and (b) primitive mantle-normalized trace element patterns for the Jiancaowan Porphyry. Chondrite and primitive mantle data after McDonough & Sun (1995).

https://doi.org/10.1017/S0016756812000283 Published online by Cambridge University Press

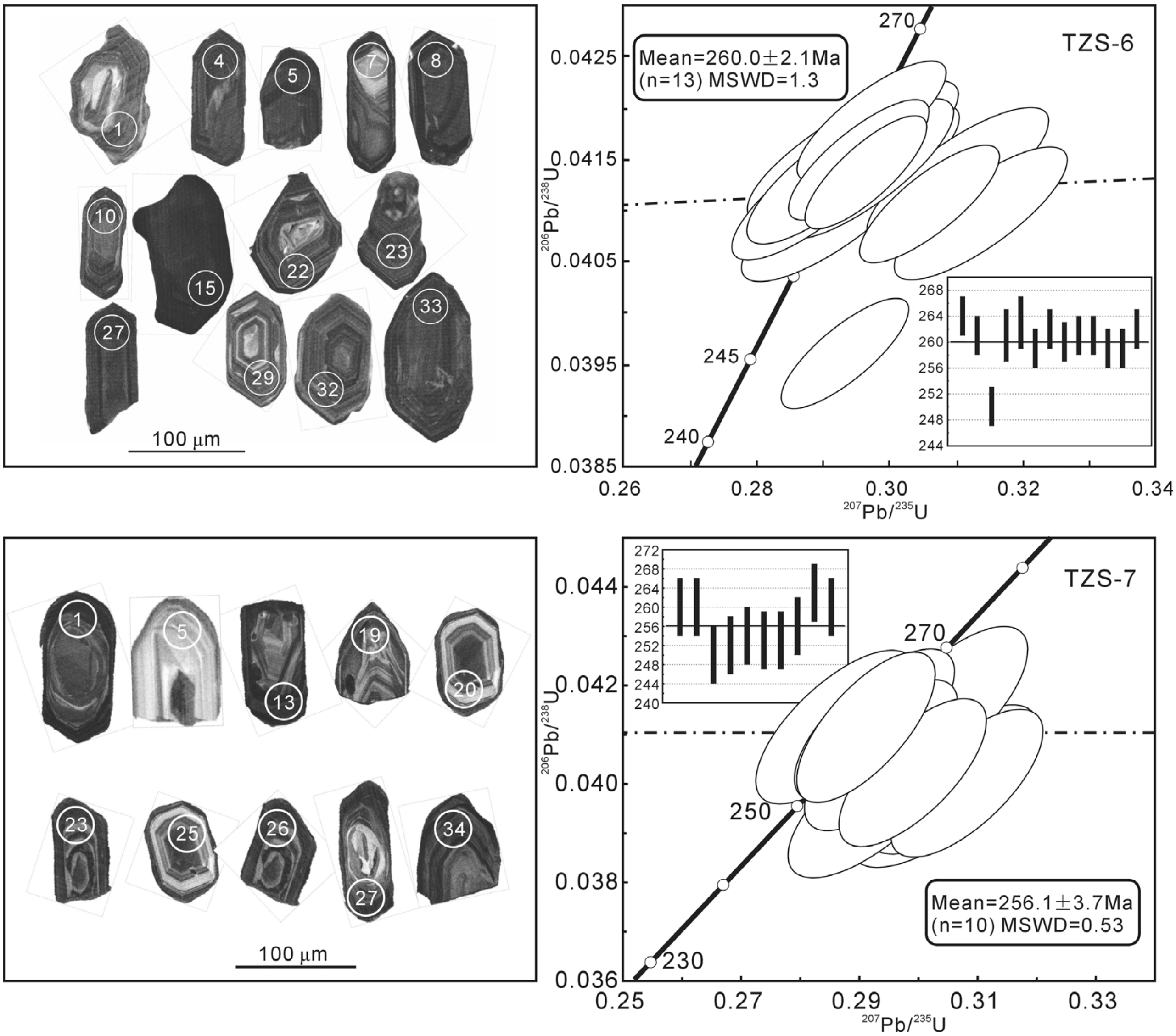

Figure 11. CL images and LA-ICP-MS U–Pb zircon concordia diagrams for the Tianzishan Monzogranite; ellipse dimensions are 2σ.

Zircon CL images and U–Pb isotopic results for Sample JCW-1 collected from the Jiancaowan Porphyry are presented in Figure 12 and the isotope data are listed in Table 3. Most zircons from the sample are euhedral, stubby to elongate prisms and range from 50 to 300 µm in size, with oscillatory zoning and core-mantle overgrowth relationships. A total of 29 analyses were carried out on 29 zircons, of which two analyses (34 and 38) gave Palaeoproterozoic ^{207}Pb–^{206}Pb ages of 1701 ± 38 Ma and 1867 ± 39 Ma; four analyses (10, 11, 21 and 35) gave ^{206}Pb–^{238}U ages of 799 ± 3 Ma, 767 ± 11 Ma, 727 ± 9 Ma and 796 ± 10 Ma. These six ages analysed on zircon cores are all concordant, and are interpreted as inherited or xenocrystic zircons. The remaining 23 analyses have contents of 55.0–2076 ppm U and 32.5–641 ppm Th, with Th/U ratios of 0.17–1.43 (indicative of a magmatic origin). The ^{206}Pb–^{238}U ages for the sample vary from 226 ± 3 to 232 ± 4 Ma and yield a weighted mean age of 229.2 ± 1.2 Ma (MSWD = 0.27, 2σ), which is interpreted as the crystallization age for the Jiancaowan Porphyry.

6.c. Zircon Hf isotope compositions

The *in situ* zircon Hf isotopic data for Sample TZS-6 are shown in Table 4 and Figure 13a, b. Eleven analyses have $^{176}Lu/^{177}Hf$ ratios of 0.000501–0.001344, and $^{176}Hf/^{177}Hf$ ratios of 0.282216–0.282470. The calculated $\varepsilon_{Hf}(t)$ is between −14.1 and −5.1 (with a weighted mean of −9.3 ± 1.7), and the two-stage Hf model age (T_{DM2}) ranges from 1345 to 1798 Ma (with a weighted mean of 1551 Ma).

The *in situ* zircon Hf isotopic data for Sample JCW-1 are shown in Table 4 and Figure 13c, d. A total of 15 analyses have $^{176}Lu/^{177}Hf$ ratios of 0.000725–0.002233, and $^{176}Hf/^{177}Hf$ ratios of 0.281859–0.282489. The calculated $\varepsilon_{Hf}(t)$ values vary between −27.5 and −5.2, and its two-stage Hf model age (T_{DM2}) ranges from 1321 Ma to 2448 Ma. Except for the maximum and minimum, the remaining 13 grains vary in a relative narrow range, with $^{176}Hf/^{177}Hf$ ratios of 0.282043–0.282399, and $\varepsilon_{Hf}(t)$ values between −21.0 and −8.4 with a weighted mean of −15.1 ± 3.1. The calculated two-stage Hf model age

https://doi.org/10.1017/S0016756812000283 Published online by Cambridge University Press

Table 4. LA-ICP-MS zircon Hf isotopic compositions for the Tianzishan Monzogranite and Jiancaowan Porphyry

Spot no.	Age(Ma)	$^{176}Yb/^{177}Hf$	2σ	$^{176}Lu/^{177}Hf$	2σ	$^{176}Hf/^{177}Hf$	2σ	εHf(0)	εHf(*t*)	2σ	T_{DM1}	T_{DM2}	$f_{Lu/Hf}$
TZS-6 from the Tianzishan monzogranite													
1	264	0.017660	0.000124	0.000709	0.000003	0.282433	0.000042	−12.0	−6.3	1.8	1148	1408	−0.98
4	261	0.017696	0.000166	0.000720	0.000007	0.282337	0.000045	−15.4	−9.8	1.9	1282	1582	−0.98
5	250	0.011454	0.000136	0.000501	0.000005	0.282387	0.000068	−13.6	−8.2	2.6	1206	1493	−0.98
7	261	0.020050	0.000191	0.000821	0.000007	0.282374	0.000057	−14.1	−8.5	2.3	1234	1517	−0.98
15	262	0.020998	0.000205	0.000919	0.000007	0.282338	0.000051	−15.4	−9.8	2.1	1288	1582	−0.97
22	260	0.015682	0.000138	0.000637	0.000005	0.282368	0.000043	−14.3	−8.7	1.8	1236	1526	−0.98
23	261	0.021248	0.000229	0.000845	0.000008	0.282311	0.000042	−16.3	−10.7	1.8	1322	1629	−0.97
27	261	0.020440	0.000118	0.000882	0.000005	0.282470	0.000050	−10.7	−5.1	2.1	1103	1345	−0.97
29	259	0.035186	0.000500	0.001344	0.000019	0.282273	0.000055	−17.6	−12.2	2.2	1394	1702	−0.96
32	259	0.012677	0.000088	0.000554	0.000003	0.282216	0.000044	−19.6	−14.1	1.9	1443	1798	−0.98
33	262	0.015406	0.000071	0.000702	0.000003	0.282392	0.000047	−13.5	−7.8	2.0	1206	1484	−0.98
JCW-1 from the Jiancaowan quartz syenite porphyry													
2	229	0.026167	0.000687	0.001054	0.000024	0.282142	0.000037	−22.3	−17.4	1.7	1565	1942	−0.97
3	231	0.044267	0.000503	0.001772	0.000020	0.282043	0.000042	−25.8	−21.0	1.8	1736	2124	−0.95
4	226	0.040712	0.000154	0.001692	0.000006	0.282238	0.000037	−18.9	−14.2	1.7	1457	1777	−0.95
5	229	0.027176	0.000378	0.001058	0.000014	0.282489	0.000045	−10.0	−5.2	1.9	1081	1321	−0.97
8	228	0.027632	0.000409	0.001171	0.000018	0.281859	0.000038	−32.3	−27.5	1.7	1965	2448	−0.96
9	230	0.031079	0.000356	0.001243	0.000013	0.282111	0.000037	−23.4	−18.5	1.7	1618	2000	−0.96
15	232	0.027166	0.000224	0.001156	0.000009	0.282342	0.000024	−15.2	−10.3	1.3	1290	1584	−0.97
18	230	0.032738	0.000105	0.001344	0.000003	0.282305	0.000035	−16.5	−11.7	1.6	1348	1653	−0.96
20	228	0.023637	0.000156	0.000989	0.000008	0.282051	0.000030	−25.5	−20.7	1.5	1690	2106	−0.97
22	227	0.026134	0.000145	0.001115	0.000005	0.282399	0.000025	−13.2	−8.4	1.4	1209	1484	−0.97
32	227	0.053133	0.000554	0.002075	0.000020	0.282305	0.000032	−16.5	−11.8	1.5	1376	1660	−0.94
33	229	0.016167	0.000277	0.000725	0.000009	0.282043	0.000023	−25.8	−20.9	1.3	1689	2117	−0.98
39	229	0.038693	0.000406	0.001442	0.000011	0.282220	0.000031	−19.5	−14.7	1.5	1473	1807	−0.96
43	232	0.028408	0.000660	0.001154	0.000026	0.282303	0.000023	−16.6	−11.7	1.3	1345	1655	−0.97
44	229	0.060253	0.001959	0.002233	0.000063	0.282196	0.000028	−20.4	−15.7	1.4	1539	1855	−0.93
21	727	0.079735	0.000483	0.003157	0.000018	0.282186	0.000031	−20.7	−6.2	1.5	1593	1775	−0.90

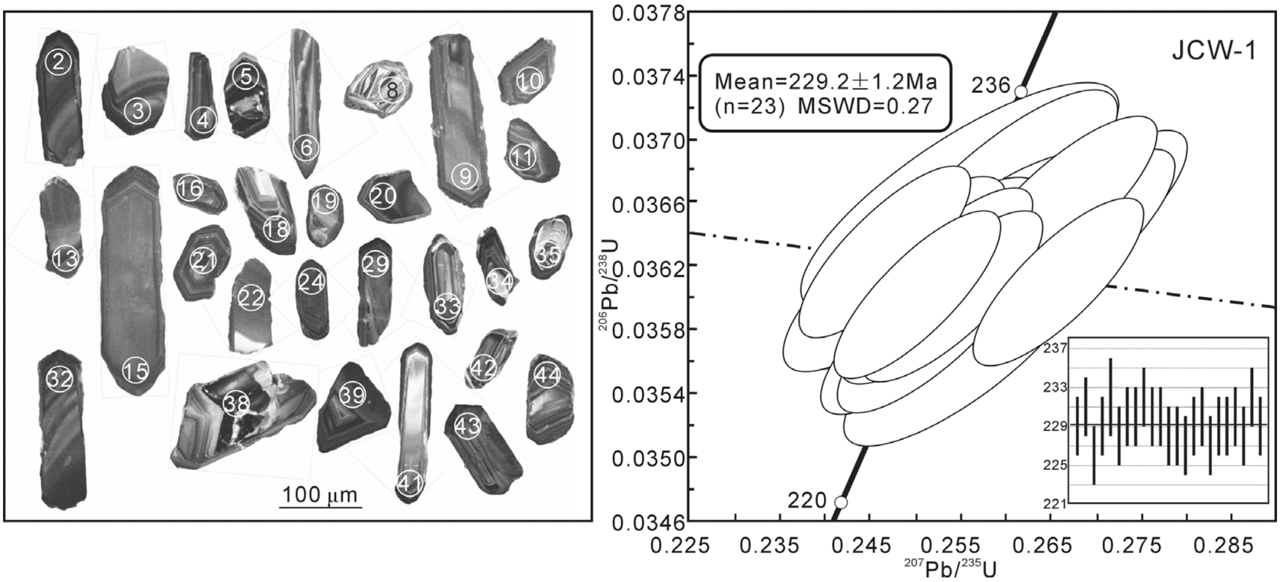

Figure 12. CL images and LA-ICP-MS U–Pb zircon concordia diagram for the Jiancaowan Porphyry; ellipse dimensions are 2σ.

(T_{DM2}) ranges from 1484 to 2124 Ma with a weighted mean of 1828 Ma. Analyses of the inherited zircon '21' gives a $^{176}Hf/^{177}Hf$ ratio of 0.282186, an $\varepsilon_{Hf}(t)$ value of −6.2 and a T_{DM2} of 1775 Ma.

7. Discussion

7.a. Petrogenesis of the Tianzishan Monzogranite

The Tianzishan Monzogranite has an unusual REE distribution relative to normal granites (Fig. 9a, b). As mentioned in Section 6.a, some samples have pronounced positive Eu anomalies, but the others have negative Eu anomalies. These features suggest that: (1) fractional crystallization processes took place during the ascent of magma (Wu *et al.* 2003; He *et al.* 2011); or (2) the differences reflect the function of temperature and oxygen fugacity in natural silicate systems (Weill & Drake, 1973; Drake & Weill, 1975). Generally, the first option would produce strong correlation trends between some elements (Wu *et al.* 2003; He *et al.* 2011). For the Tianzishan Monzogranite, the positive Eu anomalies and the absence of a correlation between Ba and Sr indicate that fractional crystallization of plagioclase is not significant. Also, there is no clear correlation between the REEs, Eu, Eu/Eu* and P_2O_5,

https://doi.org/10.1017/S0016756812000283 Published online by Cambridge University Press

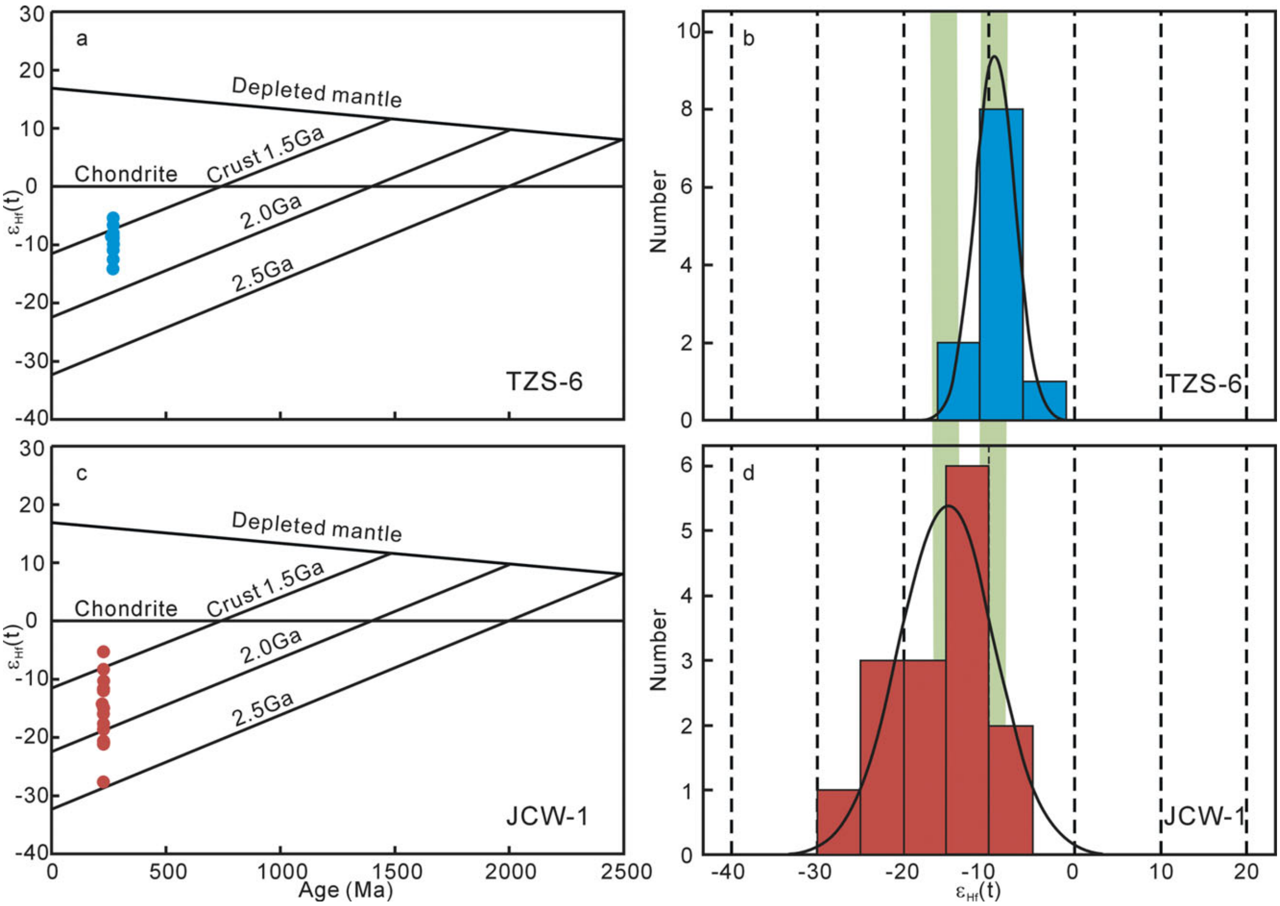

Figure 13. (Colour online) Zircon Hf isotopic compositions of the Tianzishan Monzogranite TZS-6 (a, b) and Jiancaowan quartz syenite porphyry JCW-1 (c, d). The $\varepsilon_{\text{Hf}}(t)$ of each zircon was calculated at its U–Pb age.

suggesting that the fractionation of REE-enriched minerals (e.g. monazite and apatite) is negligible. Thus, we conclude that fractional crystallization may not account for the distinct positive Eu anomalies. On the other hand, because Eu^{2+} is significantly more compatible in plagioclase than Eu^{3+} (and other REEs), the partition of Eu between plagioclase and magmatic liquid is a function of the ratio of Eu^{2+} and Eu^{3+}. A model equation shows that decreasing oxygen fugacity and temperature could result in a significantly positive Eu anomaly in natural plagioclase crystals (Weill & Drake, 1973). Therefore, it is most likely that the positive Eu anomaly in the monzogranite may be a result of its low oxygen fugacity and crystallization temperature.

The Tianzishan Monzogranite plots in the upper right corner of the high-K (calc-alkaline) field on the SiO_2–K_2O diagram (Fig. 8a). Calc-alkaline granites of intermediate to felsic chemistry are usually generated by partial melting of mafic to intermediate igneous sources (Petford & Atherton, 1996; Petford & Gallagher, 2001). However, the Tianzishan Monzogranite has high SiO_2, Al_2O_3 and K_2O contents and low MgO and Na_2O contents with high K_2O/Na_2O ratios, which is different from the magmas derived directly from lower crustal mafic rocks that usually have high Na_2O (> 4.3 wt %) contents rather than high K_2O contents (Rapp & Watson, 1995). In contrast, the major element compositions of the monzogranite are similar to the melts derived from K-rich metasedimentary rocks in many ways (Patinõ-Douce & Harris, 1998), indicating that the source of the monzogranite might comprise any K- and Al-rich and Ca-poor sedimentary rocks, which is also supported by the low CaO/Na_2O and high Al_2O_3/TiO_2 ratios of the monzogranite (Sylvester, 1998). Thus, the felsic parental magma appears to be the result of the partial melting of mixed protoliths that are composed of mafic igneous and lesser K- and Al-rich and Ca-poor sedimentary sources. The monzogranite shows spikes in Rb, Th, U and K, and troughs in Nb, Ta and Ti, which are common features of the continental crust derived from chemical differentiation of arc-derived magmas (Taylor & Mclennan, 1995). Combined with the fact that the monzogranite has evolved zircon Hf isotopic compositions with $\varepsilon_{\text{Hf}}(t)$ of −14.1 to −5.1 (Fig. 13a, b) and two-stage Hf model ages (T_{DM2}) of 1345 to 1798 Ma, we argue that the monzogranite is derived from the partial melting of Middle–Late Proterozoic crust that consists of mafic igneous and lesser sedimentary successions.

The Tianzishan Monzogranite has high Sr contents between 196 and 631 ppm, which can be attributed to the melting of a plagioclase-rich source, and the concave-upward REE patterns without significant

https://doi.org/10.1017/S0016756812000283 Published online by Cambridge University Press

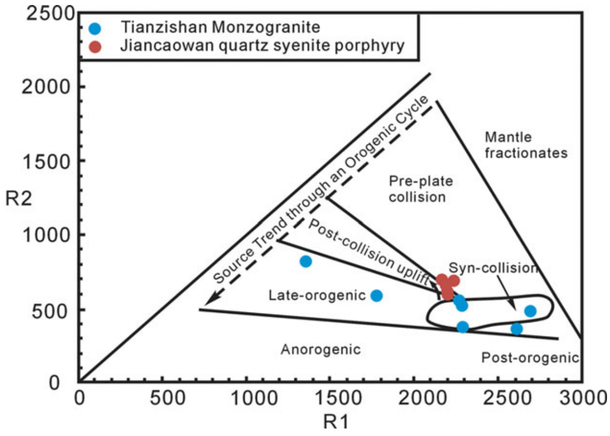

Figure 14. (Colour online) R1 versus R2 diagrams for the Tianzishan Monzogranite and Jiancaowan Porphyry (base map after Batchelor & Bowden, 1985). R1 = 4Si − 11(Na + K) − 2(Fe + Ti); R2 = 6Ca + 2Mg + Al.

Eu anomalies (average Eu/Eu* = 1.15) suggest the presence of amphibole restite (Tepper *et al.* 1993). Furthermore, the depleted HREE patterns, and low Y (2.23–19.6 ppm) and Yb (0.20–2.01 ppm) contents with low Y/Yb (9.75–13.3) and $(Ho/Yb)_N$ (1.02–1.30) ratios, indicate that the melt-restite includes garnet and amphibole (Petford & Atherton, 1996; Moyen, 2009). Experimental studies proved that the garnet-in boundaries are 0.9 to 1.4 GPa corresponding to about ∼ 45 km in depth, if the garnet-bearing granulite facies act as melt-restite for partial melting of different source rocks towards the base of a thickened crust (Vielzeuf & Schmidt, 2001; Ge *et al.* 2002). In the R1–R2 diagram of Batchelor & Bowden (1985), which reflects a complete orogenic cycle, most samples of the monzogranite plot within the area of syn-collisional granite (Fig. 14). The monzogranite yields zircon U–Pb ages of 256.1 ± 3.7 to 260.0 ± 2.1 Ma. In this period, when the Palaeo-Shangdan Ocean and Erlangping back-arc basin were closing, terminating subduction, the collision of the North and South China cratons began (Meng & Zhang, 2000; Zhang *et al.* 2001). Meanwhile, the northward subduction of the Palaeo-Mianlue Ocean located on the southern side of the Qinling Orogen was continuing (Zhang *et al.* 2001, 2004; Ratschbacher *et al.* 2003; Lai *et al.* 2004). Therefore, the Qinling Orogen was located in a regionally compressive tectonic setting during 260 to 256 Ma (the age of the monzogranite).

The Tianzishan Monzogranite is elongated parallel to the regional trend of the Shangdan Suture and its shape is coincident with the result of analogue experiments conducted to study the emplacement of granitic plutons during horizontal compression (Montanari *et al.* 2010). Hence, based on both the geological and geochemical characteristics mentioned above, we suggest that the Tianzishan Monzogranite is a syn-collisional granite and originated from the partial melting of a thickened crust formed during the collision of the North and South China cratons.

7.b. Petrogenesis of the Jiancaowan Porphyry

The Jiancaowan Porphyry has low SiO_2 (64.62–67.37 wt %) and high MgO contents (0.85–2.08 wt %) with Mg no. ranging from 43.4 to 58.2, weakly negative Eu anomalies (Eu/Eu* = 0.85–0.91), and low Fe_2O_3/MgO (1.67–3.03) and Rb/Sr (0.21–0.47) ratios, which are characteristics indicative of an unremarkable assimilation-fractional crystallization (AFC) process during the quartz syenite's ascent (Li *et al.* 2007). The A/CNK values for all of the samples have a narrow range between 0.92 and 1.08 (Fig. 8b), which indicates that the porphyry is metaluminous (e.g. Shand, 1947). The composition of the quartz syenite porphyry, together with its hornblende content, suggests that it has a high-K calc-alkaline composition.

Geochemical (e.g. Petford & Atherton, 1996; Petford & Gallagher, 2001) and experimental studies (e.g. Beard & Lofgren, 1991; Wolf & Wyllie, 1994; Rapp & Watson, 1995; Sisson *et al.* 2005) proved that calc-alkaline granites of intermediate to felsic composition are generally generated by partial melting of mafic or intermediate igneous rocks. The Jiancaowan Porphyry exhibits marked enrichment in large-ion lithophile elements (LILEs) (e.g. Rb, Th, U and K) and depletion in high-field-strength elements (HFSEs) (e.g. Nb, Ta and Ti), which is consistent with the involvement of crustal components (Taylor & Mclennan, 1995). In addition, the granite yields a zircon U–Pb age of 229.2 ± 1.2 Ma and has negative zircon $\varepsilon_{Hf}(t)$ values of −21.0 to −8.4 (T_{DM2} = 1484 to 2124 Ma) that fall within the range of typical crust (Fig. 13c, d). This indicates that the porphyry was mainly derived by partial melting of ancient mafic crust rather than juvenile basaltic underplate. The inherited zircons in the granite with Neoproterozoic (799 ± 3 Ma, 767 ± 11 Ma, 727 ± 9 Ma and 796 ± 10 Ma) and Palaeoproterozoic (1701 ± 38 Ma and 1867 ± 39 Ma) U–Pb ages provide further evidence for their magma sources. Generally, it is accepted that the South Qinling Terrane was rifted away from the South China Craton during the opening of the Palaeo-Mianlue Ocean (a branch of the Palaeo-Tethys Ocean) during Late Palaeozoic time (Meng & Zhang, 1999; Zhang *et al.* 2001; Dong *et al.* 2011). Therefore, the basement (i.e. the source of the Jiancaowan Porphyry) in the WQO has an affinity with the South China Craton (Zhang *et al.* 2007). Li *et al.* (1999, 2003) suggested that Neoproterozoic igneous rocks in the periphery of the South China Craton resulted from pre-rift magmatism at *c.* 820 Ma and syn-rift magmatism at *c.* 740 to 780 Ma, in association with the break-up of the supercontinent Rodinia. The Palaeoproterozoic ages of inherited zircons are consistent with previous zircon U–Pb dates for Palaeoproterozoic metamorphic magmatic events on the northern edge of the South China Craton (Zhang *et al.* 2006; Zheng & Zhang, 2007). Consequently, we argue that the parental magma for the porphyry mainly originated from partial melting of Neoproterozoic igneous rocks and Palaeoproterozoic metamorphic rocks.

https://doi.org/10.1017/S0016756812000283 Published online by Cambridge University Press

However, the Jiancaowan Porphyry has MgO contents and Mg no. values that are higher than the values of experimental melts from metabasalts at given SiO_2 contents (Rapp & Watson, 1995; Rapp *et al.* 1999; Xiong, Adam & Green, 2005). Therefore, high-Mg components (i.e. mantle-derived melts) must have been involved in its formation. In the WQO, many granites contain abundant mafic microgranular enclaves (MMEs) derived from partial melting of subcontinental lithospheric mantle (SCLM; Qin *et al.* 2009, 2010; Zhu *et al.* 2011). The addition of SCLM-derived melts can account for the high Mg no. values of the granites of the study area compared with experimental melts from metabasalts (e.g. Mishuling monzogranite with Mg no. = 47.6–50.7, Qin *et al.* 2009; Yangba monzogranite with Mg no. = 51–55, Qin *et al.* 2010; Wenquan porphyritic monzogranite with Mg no. = 40.05–56.34, Zhu *et al.* 2011). Considering the mixing/mingling process involving mafic and felsic magma was commonplace in the WQO (e.g. Qin *et al.* 2009, 2010; Zhu *et al.* 2011), it is likely that mixing of granitic and lesser SCLM-derived mafic magmas resulted in the high Mg no. of the porphyry. The mixing may be a factor that widened the variation in Hf isotope compositions. However, the zircon Hf model ages are all significantly older than the crystallization ages, precluding the SCLM-derived mafic magma from playing an important role in the granite origin.

On the R1–R2 diagram of Batchelor & Bowden (1985; Fig. 14), the Jiancaowan Porphyry appears to plot in a transition zone between the syn-collisional and post-collisional granitic fields. Regionally, the Qinling Orogen formed during continent–continent collision between the South and North China cratons following the closure of the Mianlue Ocean during Late Triassic time (Meng & Zhang, 1999; Zhang *et al.* 2001; Dong *et al.* 2011). With the closure of the Mianlue Ocean, the South China Craton was dragged beneath the North China Craton, resulting in UHP metamorphism forming the Dabie–Sulu UHP Zone to the east, which contains abundant diamond- and coesite-bearing eclogites (Ames, Tilton & Zhou, 1993; Hacker *et al.* 1998; Zheng, 2008). Based on a comprehensive overview of a large geochronological dataset, Zheng (2008) proposed that the Dabie–Sulu UHP Zone was formed during Middle Triassic time (240 to 225 Ma), and the peak period of collision between the North and the South China cratons took place during 235–238 Ma.

The crystallization age for the Jiancaowan Porphyry is slightly younger than peak collision, and close to the zircon U–Pb 230–205 Ma age for post-collisional high-K calc-alkaline granitic plutons that are widely distributed in the WQO (Sun *et al.* 2002; Zhang *et al.* 2005; Zhang, Wang & Wang, 2008; Gong *et al.* 2009; Qin *et al.* 2009, 2010; Jiang *et al.* 2010; Zhu *et al.* 2011). Thus, the Jiancaowan Porphyry is included with the post-collisional granites that formed during the post-collisional stage of the Qinling Orogen. In the period of tectonic transition from compression to extension, it has been postulated that local asthenosphere upwelling resulted from slab break-off (Davies & von Blankenburg, 1995; Sun *et al.* 2002; Qin *et al.* 2009, 2010; Zhu *et al.* 2011) or delamination of a thickened crust in the Qinling Orogen (Gao *et al.* 1999; Zhang *et al.* 2005; Zhang, Wang & Wang, 2008). Such underplating would cause thermal pulses that may trigger the onset of the partial melting of crustal material forming the magma for the emplacement of the Jiancaowan Porphyry.

7.c. Genesis and geotectonic setting of the Liziyuan goldfield

Mineralization in the Liziyuan goldfield formed as an integral part of the evolution of the Qinling Orogen following collision of the North and South China cratons. The structural, metamorphic and mineralogical characteristics of the mineralization are consistent with those of orogenic gold deposits throughout the world (McCuaig & Kerrich, 1998; Groves *et al.* 1998, 2003; Ridley & Diamond, 2000; Goldfarb, Groves & Gardoll, 2001; Goldfarb *et al.* 2005). In more detail: (1) the deposits are located in the Qinling Orogen that records two episodes of collision between the South and North China cratons (Fig. 1); (2) host rocks to the mineralization are a suite of metavolcanic rocks that are regionally deformed and metamorphosed to greenschist facies (Fig. 2); (3) the mineralization is hosted by reactivated ductile-brittle transtensional faults formed during the second deformation (D_2) event (Fig. 4); and (4) there are three types of primary fluid inclusions in auriferous quartz veins in the goldfield, including carbonic, mixed CO_2–H_2O and aqueous inclusions (Figs 5, 6). The common coexistence of aqueous, CO_2–H_2O and carbonic inclusions suggests that the inclusions represent the heterogeneous trapping of immiscible fluids (Fig. 5). Furthermore, microthermometric data and Laser Raman analyses suggest that the mineralization was deposited from H_2O–CO_2–$NaCl \pm CH_4$ fluids at 240° to 280 °C with a low salinity of 2.2 to 9.1 wt % NaCl equiv. (Fig. 6; Table 1).

These characteristics of the mineralization in the Liziyuan goldfield are similar to the majority of Archaean, Proterozoic and Phanerozoic orogenic gold deposits in greenschist-facies terranes throughout the world. Furthermore, like almost all orogenic deposits in the world, the deposits in the Liziyuan goldfield are proximal to granitic plutons (such as the Jiancaowan Porphyry), although a genetic relationship remains elusive (Pirajno & Bagas, 2008). Somewhat different are the locally high Pb (up to 13.3 wt %) and Cu (average 0.15 wt %) contents in the goldfield, and low Au/Ag ratios (mostly < 1). These features are similar to intrusion-related gold deposits that reflect that the gold mineralization is genetically linked to the associated granitoids (Lang & Baker, 2001; Groves *et al.* 2003), although there is a continuum between orogenic and intrusion-related gold deposits, which Pirajno & Bagas (2008) group as 'orogenic

https://doi.org/10.1017/S0016756812000283 Published online by Cambridge University Press

and intrusion-related' deposits. In addition, structurally controlled and hydrothermal deposits of Ag(–Pb–Zn), Pb–Zn(–Ag) and Cu have been recognized in the Qinling Orogen and classified as orogenic deposits (Chen, Pirajno & Sui, 2004; Chen, 2006; Zhang *et al*. 2011). Thus, these characteristics exhibited in the region are the products of metamorphic fluids developed during orogenic activity in the Qinling Orogen, and the mineralization in Liziyuan goldfield is best classified as an orogenic gold deposit.

The metallogenesis of the gold deposits in the WQO is controversial, but there was no doubt that the majority of the deposits were formed after the closure of the Palaeo-Tethys Qinling Ocean (Mao *et al*. 2002; Chen *et al*. 2004). In this study, we dated the Tianzishan Monzogranite and the Jiancaowan Porphyry with zircon U–Pb ages of 256.1 ± 3.7 to 260.0 ± 2.1 Ma and 229.2 ± 1.2 Ma, respectively. There are clear differences in the crystallization ages, petrogenesis and tectonic setting of these two plutons. Although the Tianzishan Monzogranite is one of the important host rocks for the deposits in the Liziyuan goldfield, some orebodies cut the Jiancaowan Porphyry, which is 30 Ma younger than the Tianzishan Monzogranite (Fig. 4). This indicates that the monzogranite pre-dates gold mineralization. Similarly, other pre-ore plutons have already been identified at the Ma'anqiao, Yangshan and Liba gold deposits in the WQO (Yang *et al*. 2006; Zhu *et al*. 2009*b*, 2010; Zeng *et al*. 2012). Besides, the Jiancaowan Porphyry and orebodies in the goldfield are controlled by the NW-striking transtensional faults, indicating that the mineralization age is coeval with or slightly post-dates the emplacement of the quartz syenite porphyry.

Orogenic gold deposits in many other regions have widely exposed granitic plutons, e.g. the Archaean Yilgarn Craton in Australia (Duuring, Cassidy & Hagemann, 2007), the Palaeoproterozoic North Australian Craton (Pirajno & Bagas, 2008), the Archaean Jiaodong Peninsula in China (Qiu *et al*. 2002; Mao *et al*. 2008*a*) and the Cretaceous Chugach Terrane of southern Alaska (Goldfarb *et al*. 2005). The spatially and temporally associated relationship between granites and orogenic gold deposits is an important issue that remains unresolved (Groves *et al*. 2003; Goldfarb *et al*. 2005; Duuring, Cassidy & Hagemann, 2007), but it appears that the emplacement of granites and mineralization are related to orogenic events operating at middle-crustal or shallower levels.

Hypothesized connections between hydrothermal gold deposits and Late Triassic granites have also been widely argued for the WQO (Mao *et al*. 2002; Chen *et al*. 2004; Yang *et al*. 2006; Yin & Yin, 2009; Zhang *et al*. 2009; Zhu *et al*. 2010). There are only a few reliable ages reported for gold deposits in this region until now, but gold mineralization partly overlaps the dominant 230 to 205 Ma period of magmatism within the region, such as the Liba gold deposit (quartz Ar–Ar age of 211 Ma; Feng *et al*. 2003), Xiaogouli gold deposit (Ar–Ar age on quartz of 197 Ma; Shao & Wang, 2001), Baguamiao gold deposit (233 Ma Ar–Ar age on quartz; Feng *et al*. 2002), Yangshan gold deposit (where granite is present in the mining area and mineralization is associated with monazite Th–U–Pb ages of 220 Ma and 190 Ma; Yang *et al*. 2006), Yindonggou Ag–Au deposit (fluid inclusions in quartz with Rb–Sr isochron age of 205 Ma and muscovite K–Ar age of 216 Ma; Li *et al*. 2011) and Xujiapo Au–Ag deposit (tremolite and biotite with K–Ar ages of 218 Ma and between 224 and 211 Ma; Li *et al*. 2011). A recent geochronological study on the Liba gold deposit obtained similar ages. SHRIMP U–Pb zircon ages of the pre-mineralization granitic dykes from the Liba gold deposit are between 222 Ma and 217 Ma, the Ar–Ar age of post-mineralization lamprophyre dykes is 215 Ma and Ar–Ar dating on mica associated with gold mineralization yielded an age of 216 Ma (Zeng *et al*. 2012). All of these gold deposits are structurally controlled and were derived from low-salinity and CO_2-rich fluids with enriched oxygen and sulfur isotopic compositions (Mao *et al*. 2002; Chen *et al*. 2004). Moreover, there is no known granitic composition that is proven to be the source for gold mineralization, suggesting that magmatic-hydrothermal fluids do not fully account for the genesis of these gold deposits in the region. Hence, the metamorphic fluids produced by regional metamorphism related to collisional orogenesis of the WQO are here advocated for the gold metallogenesis (Mao *et al*. 2002; Chen *et al*. 2004; Zhu *et al*. 2010). Furthermore, in the WQO, the feldspar multiple diffusion domain (MDD) and apatite fission track methods revealed 230 to 210 Ma was a major period for regional rapid cooling (Zheng *et al*. 2004). It is suggested that the Late Triassic magmatism and gold mineralization are synchronous. Thus, it is possible that the spatial concomitance of plutons and gold deposits is largely due to their both being products of collisional processes (Groves *et al*. 1998; Goldfarb *et al*. 2005; Duuring, Cassidy & Hagemann, 2007).

It has been suggested that during the initial collision of an orogenic wedge with a continent, major compressional stresses can be transmitted into the continent as a consequence of subduction resistance, giving rise to large-scale intraplate deformations and strike-slip shear zones (Ziegler, van Wees & Cloetingh, 1998; Rezaei-Kahkhaei *et al*. 2010). Similarly, Triassic collisional orogenesis of the Qinling Orogen produced intensive brittle-ductile shearing deformation and greenschist-facies metamorphism in the WQO (Zhang *et al*. 2001, 2004; Dong *et al*. 2011). The deformation and metamorphism is marked by the NW-striking ductile dextral strike-slip faults (D_1) and greenschist-facies metavolcanic rocks in the Liziyuan goldfield in this study. Some Triassic metamorphic ages for different lithologies in the South Qinling Terrane have been reported in the literature (between 233 and 216 Ma for Mianlue Blueschist, Mattauer *et al*. 1985, and 242 to 221 Ma for Mianlue Ophiolite, Li *et al*. 1996). Recently, detailed thermochronology studies proposed

https://doi.org/10.1017/S0016756812000283 Published online by Cambridge University Press

the time of transpressive slip along the shear/fault zones (Lo-Nan, Shang-Xiang and Shangdan) of the Qinling Orogen was 240 to 200 Ma, with deformation temperatures reaching 100 to 300 °C and locally higher but < 400 °C (Ratschbacher *et al.* 2003). Owing to the relatively high geothermal gradients and regionally prograde metamorphism during convergent processes, water, silica and volatiles such as CO_2 were liberated and likely mobilized during devolatilization processes forming metamorphic fluids characterized by being medium temperature, low salinity and CO_2 rich, and enriched in oxygen and sulfur isotope compositions (Groves *et al.* 1998, 2003; Ridley & Diamond, 2000). Therefore, collisional orogenesis of the Qinling Orogen may drive large-scale generation and transport of hydrothermal fluids that could have mobilized and extracted ore elements from the wall rocks along their flow pathways.

The Liziyuan goldfield is spatially and temporally associated with Late Triassic post-collisional quartz syenite assigned to the Jiancaowan Porphyry. Detailed mapping revealed that there is exposed a large amount of Jurassic red sandstone and conglomerate, which unconformably overlies pre-Jurassic strata, in normal fault controlled rift basins in the WQO (Zhang *et al.* 2001; Dong *et al.* 2011). The occurrence of these rift basins suggests that the WQO had already evolved into extension or post-orogenic collapse after the collision. Therefore, considering this geological detail, it is reasonable to deduce that intensive geotectonic activity and relevant gold deposit formation took place in the transitional stage (i.e. change in tectonic regime from compression to extension) of the Qinling Orogen (Chen *et al.* 2004). According to the pressure–temperature (*P–T*) paths of collisional orogenesis, a complete collisional-orogenic cycle usually includes three stages: (1) an early stage of compression with increasing pressure and temperature; (2) a middle transition stage from compression to extension with decreasing pressure and increasing temperature; and (3) a late extension stage with decreasing pressure and temperature (Jamieson, 1991; Chen *et al.* 2004, 2008; Zhu *et al.* 2010). In the transition stage from compression to extension, the orogen is in the special tectonic situation involving decompression while pressure decreases and temperature increases, which would have facilitated partial melting, fluid generation and metallogeny in the orogenic belt (Chen *et al.* 2008). Such conditions together with asthenosphere upwelling provide sufficient heat for partial melting of the crust that formed the magma forming the Jiancaowan Porphyry, and hydrothermal fluid fluxes that are necessary for gold mineralization. At the same time, the faults in the Liziyuan goldfield would have dilated due to a regional decrease in pressure at the transition stage; these would have been extremely critical conduits and precipitation places for hydrothermal fluids (Kang & Han, 2003). When the ore-forming fluids migrated into the transtensional faults and microscopic fractures of the host rocks, the rapid change in physicochemical conditions would result in sulphide precipitation and the formation of economic mineralization.

8. Conclusions

Our studies of plutons and mineralization in the Qinling Orogen show:

(1) Multi-stage magmatism took place in the Liziyuan goldfield, which is represented by the Tianzishan Monzogranite and Jiancaowan Porphyry. Both plutons are enriched in LREEs and LILEs and depleted in HFSEs, with negative zircon $\varepsilon_{\mathrm{Hf}}(t)$ values, suggesting that they are predominantly derived from the partial melting of ancient crust. The relatively high Mg no. and Cr and Ni contents for the Jiancaowan Porphyry may result from mixing with a small amount of subcontinental lithospheric mantle-derived mafic magma.

(2) The Tianzishan Monzogranite has LA-ICP-MS zircon U–Pb ages of 256.1 ± 3.7 to 260.0 ± 2.1 Ma, indicating that it belongs to the class of syn-collisional granites and formed in the regional compressive setting. In contrast, the Jiancaowan Porphyry has a LA-ICP-MS zircon U–Pb age of 229.2 ± 1.2 Ma, indicating that the granite formed in the post-collisional stage of the Qinling Orogen.

(3) The Liziyuan goldfield is contemporaneous with or slightly younger than the emplacement of the Jiancaowan Porphyry, suggesting it also formed in the post-collisional stage of the Qinling Orogen. The Late Triassic collisional orogenesis is responsible for the synchronous formation of the post-collisional magmatism and gold mineralization. In view of the geological characteristics and tectonic setting of the Liziyuan goldfield, we prefer to classify the mineralization as an orogenic gold deposit.

Acknowledgements. This study was jointly supported by the China Natural Sciences Foundation (Grant Nos. 41030423, 40872071 and 41072068), National Basic Research Programme of China (Grant No. 2006CB403502), Graduate Innovation and Creativity Funds of Northwest University, China (Grant Nos. 10DZSY06 and 10YZZ24) and MOST Special Fund from the State Key Laboratory of Continental Dynamics, Northwest University (Grant Nos. BJ11061 and BJ091349). We thank Guofen He, Mengning Dai, Kaiyun Chen and Chunrong Diwu of the State Key Laboratory of Continental Dynamics of Northwest University for their assistance in zircon U–Pb and Lu–Hf isotope analyses. Colleagues of the Liziyuan Gold Mining Company are thanked for their assistance in our field work. We are most grateful for thoughtful comments by two anonymous reviewers and Dr Phil Leat, which resulted in a significantly improved paper. Dr Leon Bagas from the Centre for Exploration Targeting, University of Western Australia, is greatly acknowledged for his critical reading, improvement and comments on the manuscript.

References

AMES, L., TILTON, G. R. & ZHOU, G. Z. 1993. Timing of collision of the Sino-Korean and Yangtse cratons: U-Pb

zircon dating of coesite-bearing eclogites. *Geology* **21**, 339–42.
ANDERSEN, T. 2002. Correction of common lead in U-Pb analyses that do not report ^{204}Pb. *Chemical Geology* **192**, 59–79.
BATCHELOR, R. B. & BOWDEN, P. 1985. Petrogenetic interpretation of granitoid rock series using multicationic parameters. *Chemical Geology* **48**, 43–55.
BEARD, J. S. & LOFGREN, G. E. 1991. Dehydration melting and water-saturated melting of basaltic and andesitic greenstones and amphibolites at 1–3 and 6–9 kb. *Journal of Petrology* **32**, 365–401.
BLICHERT-TOFT, J. & ALBARÈDE, F. 1997. The Lu-Hf isotope geochemistry of chondrites and the evolution of the mantle-crust system. *Earth and Planetary Science Letters* **148**, 243–58.
BODNAR, R. J. 1993. Revised equation and table for determining the freezing point depression of H_2O-NaCl solutions. *Geochimica et Cosmochimica Acta* **57**, 683–4.
CHEN, Y. J. 2006. Orogenic-type deposits and their metallogenic model and exploration potential. *Geology in China* **33**, 1181–96 (in Chinese with English abstract).
CHEN, Z., LU, S., LI, H., LI, H., XIANG, Z., ZHOU, H. & SONG, B. 2006. Constraining the role of the Qinling orogen in the assembly and break-up of Rodinia: tectonic implications for Neoproterozoic granite occurrences. *Journal of Asian Earth Sciences* **28**, 99–115.
CHEN, Y. J., PIRAJNO, F. & SUI, Y. H. 2004. Isotope geochemistry of the Tieluping silver-lead deposit, Henan Province, China: a case study of orogenic silver-dominated deposits and related tectonic setting. *Mineralium Deposita* **39**, 560–75.
CHEN, Y., ZHANG, J., PIRAJNO, F. & QI, J. P. 2008. The Shanggong gold deposit, Eastern Qinling Orogen, China: isotope geochemistry and implications for ore genesis. *Journal of Asian Earth Sciences* **33**, 252–66.
CHEN, Y., ZHANG, J., ZHANG, F., PIRAJNO, F. & LI, C. 2004. Carlin and Carlin-like gold deposits in Western Qinling Mountains and their metallogenic time, tectonic setting and model. *Geological Review* **50**, 134–52 (in Chinese with English abstract).
CHU, N. C., TAYLOR, R. N., CHAVAGNAC, V., NESBITT, R. W., BOELLA, R. M., MILTON, J. A., GERMAIN, C. R., BAYON, G. & BURTON, K. 2002. Hf isotope ratio analyses using multi-collector inductively coupled plasma mass spectrometry: an evaluation of isobaric interference corrections. *Journal of Analytical Atomic Spectrometry* **17**, 1567–74.
DAVIES, J. H. & VON BLANKENBURG, F. 1995. Slab breakoff: a model of lithosphere detachment and its test in the magmatism and deformation of collisional orogens. *Earth Planetary Science Letters* **129**, 85–102.
DEBIEVRE, P. & TAYLOR, P. D. P. 1993. Table of the isotopic composition of the elements. *International Journal of Mass Spectrometry and Ion Processes* **123**, 149–66.
DING, S. P., PEI, X. Z., LI, Y., HU, B., ZHAO, X. & GUO, J. F. 2004. Analyses of the disintegration and tectonic setting of the "Liziyuan Group" in the Tianshui area, western Qinling. *Geological Bulletin of China* **23**, 1219–24 (in Chinese with English abstract).
DONG, Y., ZHANG, G., NEUBAUER, F., LIU, X., GENSER, J. & HAUZENBERGER, C. 2011. Tectonic evolution of the Qinling orogen, China: review and synthesis. *Journal of Asian Earth Sciences* **41**, 213–37.
DRAKE, M. J. & WEILL, D. F. 1975. Partition of Sr, Ba, Ca, Y, Eu^{2+}, Eu^{3+}, and other REE between plagioclase feldspar and magmatic liquid: an experimental study. *Geochimica et Cosmochimica Acta* **39**, 689–712.
DUURING, P., CASSIDY, K. F. & HAGEMANN, S. G. 2007. Granitoid-associated orogenic, intrusion-related, and porphyry style metal deposits in the Archean Yilgarn Craton, Western Australia. *Ore Geology Reviews* **32**, 157–86.
ELHLOU, S., BELOUSOVA, E., GRIFFIN, W. L., PEARSON, N. J. & O'REILLY, S. Y. 2006. Trace element and isotopic composition of GJ red zircon standard by laser ablation. *Geochimica et Cosmochimica Acta* **70**, A158.
FENG, J. Z., WANG, D. B., WANG, X. M. & SHAO, S. C. 2004. Stable isotope geochemistry of three typical gold deposits in the West Qinling. *Geology in China* **31**, 78–84 (in Chinese with English abstract).
FENG, J. Z., WANG, D. B., WANG, X. M., SHAO, S. C. & LI, T. F. 2002. Geochronology of gold deposits and its implication for metallogenesis in the Fengxian-Lixian area, Qinling orogenic belt, China. *Resource Geology* **52**, 263–72.
FENG, J. Z., WANG, D. B., WANG, X. M., SHAO, S. C., MA, Z. G. & ZHANG, X. G. 2003. Geology and metallogenesis of the Baguamiao giant gold deposit in Fengxian, Shannxi province. *Acta Geologica Sinica* **77**, 387–98 (in Chinese with English abstract).
GAO, S., ZHANG, B. R., JIN, Z. M. & KERN, H. 1999. Lower crustal delamination in the Qinling-Dabie orogenic belt. *Science in China Series D: Earth Sciences* **42**, 423–33.
GE, X. Y., LI, X. H., CHEN, Z. G. & LI, W. P. 2002. Geochemistry and petrogenesis of Jurassic high Sr/low Y granitoids in eastern China: constrains on crustal thickness. *Chinese Science Bulletin* **47**, 962–8.
GOLDFARB, R. J., GROVES, D. I. & GARDOLL, S. 2001. Orogenic gold and geologic time: a global synthesis. *Ore Geology Reviews* **18**, 1–75.
GOLDFARB, R. J., BAKER, T., DUBE, B., GROVES, D. I., HART, C. J. R. & GOSSELIN, P. 2005. Distribution, character, and genesis of gold deposits in metamorphic terranes. In *Economic Geology 100th Anniversary Volume* (eds J. W. Hedenquist, J. F. H. Thompson, R. J. Goldfarb & J. P. Richards), pp. 407–50. Littleton, Colorado: Society of Economic Geologists.
GONG, H. J., ZHU, L. M., SUN, B. Y., LI, B. & GUO, B. 2009. Zircon U-Pb ages and Hf isotope characteristics and their geological significance of the Shahewan, Caoping and Zhashui granitic plutons in the South Qinling orogen. *Acta Petrologica Sinica* **25**, 248–64 (in Chinese with English abstract).
GROVES, D. I., GOLDFARB, R. J., GEBRE-MARIAM, M., HAGEMANN, S. G. & ROBERT, F. 1998. Orogenic gold deposits: a proposed classification in the context of their crustal distribution and relationship to other gold deposit types. *Ore Geology Reviews* **13**, 7–27.
GROVES, D. I., GOLDFARB, R. J., ROBERT, F. & HART, C. J. R. 2003. Gold deposits in metamorphic belts: overview of current understanding, outstanding problems, future research, and exploration significance. *Economic Geology* **98**, 1–29.
HACKER, B. R., RATSCHBACHER, L., WEBB, L., IRELAND, T., WALKER, D. & DONG, S. W. 1998. U-Pb zircon ages constrain the architecture of the ultrahigh-pressure Qinling-Dabie Orogen, China. *Earth and Planetary Science Letters* **161**, 215–30.
HE, Y. S., LI, S. G., HOEFS, J., HUANG, F., LIU, S. A. & HOU, Z. H. 2011. Post-collisional granitoids from the Dabie orogen: new evidence for partial melting of a thickened continental crust. *Geochimica et Cosmochimica Acta* **75**, 3815–38.
JAMIESON, R. A. 1991. P-T-t paths of collisional orogens. *Geologische Rundschau* **80**, 321–32.

https://doi.org/10.1017/S0016756812000283 Published online by Cambridge University Press

JIANG, Y. H., JIN, G. D., LIAO, S. Y., ZHOU, Q. & ZHAO, P. 2010. Geochemical and Sr-Nd-Hf isotopic constraints on the origin of late Triassic granitoids from the Qinling orogen, central China: implications for a continental arc to continent-continent collision. *Lithos* **117**, 183–97.

KANG, Y. L. & HAN, Y. Q. 2003. Analyses on the geological conditions and ore-controlling factors of Liziyuan gold deposit, Tianshui, Gansu. *Gansu Metallurgy* **25** (1–4), 23 (in Chinese).

LAI, S. C., ZHANG, G. W., DONG, Y. P., PEI, X. Z. & CHEN, L. 2004. Geochemistry and regional distribution of ophiolite and associated volcanics in Mianlüe suture, Qinling-Dabie Mountains. *Science in China Series D: Earth Sciences* **47**, 289–99.

LANG, J. R. & BAKER, T. 2001. Intrusion-related gold systems: the present level of understanding. *Mineralium Deposita* **36**, 477–89.

LI, N., CHEN, Y. J., FLETCHER, I. R. & ZENG, Q. T. 2011. Triassic mineralization with Cretaceous overprint in the Dahu Au-Mo deposit, Xiaoqinling gold province: constraints from SHRIMP monazite U-Th-Pb geochronology. *Gondwana Research* **20**, 543–52.

LI, J., CHEN, Y. J., LI, Q. Z., MAO, S. D., QIN, Y., GUO, J. H., NAN, Z. L. & YANG, R. S. 2008. The C-H-O isotope systematics of the Yangshan gold deposit, Gansu and its implication for the ore-fluid origin. *Acta Petrologica Sinica* **24**, 817–26 (in Chinese with English abstract).

LI, Z. X., LI, X. H., KINNY, P. D. & WANG, J. 1999. The breakup of Rodinia: did it start with a mantle plume beneath South China? *Earth and Planetary Science Letters* **173**, 171–81.

LI, Z. X., LI, X. H., KINNY, P. D., WANG, J., ZHANG, S. & ZHOU, H. 2003. Geochronology of Neoproterozoic syn-rift magmatism in the Yangtze craton, South China and correlations with other continents: evidence for a mantle superplume that broke up Rodinia. *Precambrian Research* **122**, 85–109.

LI, X. H., LI, Z. X., LI, W. X., LIU, Y., YUAN, C., WEI, G. J. & QI, C. S. 2007. U-Pb zircon, geochemical and Sr-Nd-Hf isotopic constraints on age and origin of Jurassic I- and A-type granites from central Guangdong, SE China: a major igneous event in response to foundering of a subducted flat-slab? *Lithos* **96**, 186–204.

LI, S. G., SUN, W. D., ZHANG, G. W., CHEN, J. Y & YANG, Y. C. 1996. Chronology and geochemistry of meta-volcanic rocks from Heigouxia Valley in the Mian-lue tectonic zone, South Qinling: evidence for a Paleozoic oceanic basin and its close time. *Science in China Series D: Earth Sciences* **39**, 300–10.

LIU, H. L. & AI, M. Q. 2009. Optimization of the milling and floatation parameters for Suishizi main orebody in Liziyuan mine. *Gold* **31**, 44–6 (in Chinese with English abstract).

LIU, Y. H., LIU, H. L., GAO, H. X., LI, Z. G., ZHUANG, X., ZHANG, Y. Q., ZHENG, X. Z. & WEI, J. Q. 2011. Material components and occurrence states of gold and silver in the Lizi gold deposit, Tianshui, Gansu Province. *Geology and Exploration* **47**, 837–45 (in Chinese with English abstract).

LUDWIG, K. R. 2003. *User's Manual for Isoplot/Ex Version 3.00: A Geochronological Toolkit for Microsoft Excel*. Berkeley, USA: Berkeley Geochronological Center, Special Publication 4, 73 pp.

MAO, J. W., QIU, Y. M., GOLDFARB, R. J., ZHANG, Z. C., GARWIN, S. & REN, F. S. 2002. Geology, distribution and classification of gold deposits in the western Qinling belt, central China. *Mineralium Deposita* **37**, 352–77.

MAO, J. W., WANG, Y. T., LI, H. M., PIRAJNO, F., ZHANG, C. Q. & WANG, R. T. 2008*a*. The relationship of mantle-derived fluids to gold metallogenesis in the Jiaodong Peninsula: evidence from D-O-C-S isotope systematics. *Ore Geology Reviews* **33**, 361–81.

MAO, J. W., XIE, G. Q., BIERLEIN, F., QÜ, W. J., DU, A. D., YE, H. S., PIRAJNO, F., LI, H. M., GUO, B. J., LI, Y. F. & YANG, Z. Q. 2008*b*. Tectonic implications from Re-Os dating of Mesozoic molybdenum deposits in the East Qinling-Dabie orogenic belt. *Geochimica et Cosmochimica Acta* **72**, 4607–26.

MATTAUER, M., MATTE, P. H., MALAVIEILLE, J., TAPPONNIER, P., MALUSKI, H., XU, Z. Q., LU, Y. L. & TANG, Y. Q. 1985. Tectonics of the Qinling Belt: build-up and evolution of eastern Asia. *Nature* **317**, 496–500.

MCCUAIG, T. C. & KERRICH, R. 1998. *P-T-t*-deformation-fluid characteristics of lode gold deposits: evidence from alteration systematics. *Ore Geology Reviews* **12**, 381–453.

MCDONOUGH, W. F. & SUN, S. S. 1995. The composition of the earth. *Chemical Geology* **120**, 223–53.

MENG, Q. R. & ZHANG, G. W. 1999. Timing of collision of the North and South China blocks: controversy and reconciliation. *Geology* **27**, 123–6.

MENG, Q. R. & ZHANG, G. W. 2000. Geologic framework and tectonic evolution of the Qinling orogen, central China. *Tectonophysics* **323**, 183–96.

MONTANARI, D., CORTI, G., SANI, F., VENTISETTE, C. D., BONINI, M. & MORATTI, G. 2010. Experimental investigation on granite emplacement during shortening. *Tectonophysics* **484**, 147–55.

MOYEN, J. F. 2009. High Sr/Y and La/Yb ratios: the meaning of the "adakitic signature". *Lithos* **112**, 556–74.

PATINÕ-DOUCE, A. E. & HARRIS, N. 1998. Experimental constraints on Himalayan anatexis. *Journal of Petrology* **39**, 689–710.

PEI, X. Z., LIU, H. B., DING, S. P., LI, Z. C., HU, B., SUN, R. Q. & HOU, Y. H. 2006. Geochemical characteristics and tectonic significance of the meta-volcanic rocks in the Liziyuan Group from Tianshui area, West Qinling orogen. *Geotectonica et Metallogenia* **30**, 193–205 (in Chinese with English abstract).

PETFORD, N. & ATHERTON, M. 1996. Na-rich partial melts from newly underplated basaltic crust: the Cordillera Blanca batholith, Peru. *Journal of Petrology* **37**, 1491–521.

PETFORD, N. & GALLAGHER, K. 2001. Partial melting of mafic (amphibolitic) lower crust by periodic influx of basaltic magma. *Earth and Planetary Science Letters* **193**, 483–99.

PIRAJNO, F. & BAGAS, L, 2008. A review of Australia's Proterozoic mineral systems and genetic models. *Precambrian Research* **166**, 54–80.

QIN, J. F., LAI, S. C., DIWU, C. R., JU, Y. J. & LI, Y. F. 2010. Magma mixing origin for the post-collisional adakitic monzogranite of the Triassic Yangba pluton, northwestern margin of the South China block: geochemistry, Sr-Nd isotopic, zircon U-Pb dating and Hf isotopic evidences. *Contributions to Mineralogy and Petrology* **159**, 389–409.

QIN, J. F., LAI, S. C., RODNEY, G., DIWU, C. R., JU, Y. J. & LI, Y. F. 2009. Geochemical evidence for origin of magma mixing for the Triassic monzonitic granite and its enclaves at Mishulingin the Qinling orogen (central China). *Lithos* **112**, 259–76.

QIU, Y. M., GROVES, D. I., MCNAUGHTON, N. J., WANG, L. G. & ZHOU, T. H. 2002. Nature, age, and tectonic setting of granitoid-hosted, orogenic gold deposits of the

https://doi.org/10.1017/S0016756812000283 Published online by Cambridge University Press

Jiaodong Peninsula, eastern North China craton, China. *Mineralium Deposita* **37**, 283–305.
QIU, H. N. & WIJBRANS, J. R. 2006. Paleozoic ages and excess ^{40}Ar in garnets from the Bixiling eclogite in Dabieshan, China: new insights from ^{40}Ar/^{39}Ar dating by stepwise crushing. *Geochimica et Cosmochimica Acta* **70**, 2354–70.
RAPP, R. P., SHIMIZU, N., NORMAN, M. D. & APPLEGATE, G. S. 1999. Reaction between slab-derived melts and peridotite in the mantle wedge: experimental constraints at 3.8 GPa. *Chemical Geology* **160**, 335–56.
RAPP, R. P. & WATSON, E. B. 1995. Dehydration melting of metabasalt at 8–32 kbar: implications for continental growth and crust-mantle recycling. *Journal of Petrology* **36**, 891–931.
RATSCHBACHER, L., HACKER, B. R., CALVERT, A., WEBB, L. E., GRIMMER, J. C., MCWILLIAMS, M. O., IRELAND, T., DONG, S. W. & HU, J. M. 2003. Tectonics of the Qinling (Central China): tectonostratigraphy, geochronology, and deformation history. *Tectonophysics* **366**, 1–53.
REZAEI-KAHKHAEI, M., KANANIAN, A., ESMAEILY, D. & ASIABANHA, A. 2010. Geochemistry of the Zargoli granite: implications for development of the Sistan Suture Zone, southeastern Iran. *Island Arc* **19**, 259–76.
RIDLEY, J. R. & DIAMOND, L. W. 2000. Fluid chemistry of orogenic lode-gold deposits and implications for genetic models. *Reviews in Economic Geology* **13**, 141–62.
ROEDDER, E. 1984. *Fluid Inclusions*. In (ed. P. H. Ribbe) *Reviews in Mineralogy vol. 12*. Washington DC: Mineralogical Society of America, 644 pp.
SHAND, S. J. 1947. *Eruptive Rocks, Their Genesis, Composition, Classification, and Their Relation to Ore-Deposits*, 3rd ed. New York: John Wiley and Sons, 488 pp.
SHAO, S. C. & WANG, D. B. 2001. ^{39}Ar-^{40}Ar dating of three typical gold deposits and its geological significance in the southern Qinling region. *Acta Geologica Sinica* **75**, 106–10 (in Chinese with English abstract).
SISSON, T. W., RATAJESKI, K., HANKINS, W. B. & GLAZNER, A. F. 2005. Voluminous granitic magmas from common basaltic sources. *Contributions to Mineralogy Petrology* **148**, 635–61.
SÖDERLUND, U., PATCHETT, P. J., VERVOORT, J. D. & ISACHSEN, C. E. 2004. The ^{176}Lu decay constant determined by Lu-Hf and U-Pb isotope systematics of Precambrian mafic intrusions. *Earth and Planetary Science Letters* **219**, 311–24.
SUN, W. D., LI, S. G., CHEN, Y. D. & LI, Y. J. 2002. Timing of synorogenic granitoids in the south Qinling, central China: constraints on the evolution of the Qinling-Dabie Orogenic Belt. *Journal of Geology* **110**, 457–68.
SYLVESTER, P. J. 1998. Post-collisional strongly peraluminous granites. *Lithos* **45**, 29–44.
TAYLOR, S. R. & MCLENNAN, S. M. 1995. The geochemical evolution of the continental crust. *Reviews in Geophysics* **33**, 241–65.
TEPPER, J. H., NELSON, B. K., BERGANTZ, G. W. & IRVING, A. J. 1993. Petrology of the Chilliwack batholith, North Cascades, Washington: generation of calc-alkaline granitoids by melting of mafic lower crust with variable water fugacity. *Contributions to Mineralogy and Petrology* **113**, 333–51.
VERVOORT, J. D. & BLICHERT-TOFT, J. 1999. Evolution of the depleted mantle: Hf isotope evidence from juvenile rocks through time. *Geochimica et Cosmochimica Acta* **63**, 533–56.
VERVOORT, J. D. & PATCHETT, P. J. 1996. Behavior of hafnium and neodymium isotopes in the crust: constraints from Precambrian crustally derived granites. *Geochimica et Cosmochimica Acta* **60**, 3717–33.
VIELZEUF, D. & SCHMIDT, M. W. 2001. Melting relations in hydrous systems revisited: application to metapelites, metagreywackes and metabasalts. *Contributions to Mineralogy and Petrology* **141**, 251–67.
WEILL, D. F. & DRAKE, M. J. 1973. Europium anomaly in plagioclase feldspar: experimental results and semi-quantitative model. *Science* **180**, 1059–60.
WOLF, M. B. & WYLLIE, P. J. 1994. Dehydration melting of amphibolite at 10 kbar: the effects of temperature and time. *Contributions to Mineralogy and Petrology* **115**, 369–83.
WU, F. Y., JAHN, B. M., WILDER, S. A., LO, C. H., YUI, T. F., LIN, Q., GE, W. C. & SUN, D. Y. 2003. Highly fractionated I-type granites in NE China (I): geochronology and petrogenesis. *Lithos* **66**, 241–73.
WU, Y. B., ZHENG, Y. F., ZHAO, Z. F., GONG, B., LIU, X. M. & WU, F. Y. 2006. U-Pb, Hf and O isotope evidence for two episodes of fluid-assisted zircon growth in marble-hosted eclogites from the Dabie orogen. *Geochimica et Cosmochimica Acta* **70**, 3743–61.
XIONG, X. L., ADAM, J. & GREEN, T. H. 2005. Rutile stability and rutile/melt HFSE partitioning during partial melting of hydrous basalt: implications for TTG genesis. *Chemical Geology* **218**, 339–59.
YANG, R. S., CHEN, Y. J., ZHANG, F. X., LI, Z. H., MAO, S. D., LIU, H. J. & ZHAO, C. H. 2006. Chemical Th-U-Pb ages of monazite from the Yangshan gold deposit, Gansu province and their geologic and metallogenic implications. *Acta Petrologica Sinica* **22**: 2603–10 (in Chinese with English abstract).
YIN, Y. & YIN, X. M. 2009. Porphyry Cu-Mo-Au mineralization related to adakite and Himalayan type granite in the northern margin of West Qinling. *Acta Petrologica Sinica* **25**, 1239–52 (in Chinese with English abstract).
YUAN, H. L., GAO, S., DAI, M. N., ZONG, C. L., GÜNTHER, D., FONTAINE, G. H., LIU, X. M. & DIWU, C. R. 2008. Simultaneous determinations of U-Pb age, Hf isotopes and trace element compositions of zircon by excimer laser ablation quadrupole and multiple collector ICP-MS. *Chemical Geology* **247**, 100–18.
YUAN, H. L., GAO, S., LIU, X. M., LI, H. M., GÜNTHER, D. & WU, F. Y. 2004. Accurate U-Pb age and trace element determinations of zircon by laser ablation-inductively coupled plasma mass spectrometry. *Geoanalytical and Geostandard Research* **28**, 353–70.
ZENG, Q. T., MCCUAIG, T. C., HART, J. R. C., JOURDAN, F., MUHLING, J. & BAGAS, L. 2012. Structural and geochronological studies on the Liba goldfield of the West Qinling Orogen, Central China. *Mineralium Deposita*, published online 26 January 2012. doi: 10.1007/s00126-011-0398-8.
ZHANG, J., CHEN, Y. J., YANG, Y. & DENG, J. 2011. Lead isotope systematics of the Weishancheng Au-Ag belt, Tongbai Mountains, central China: implication for ore genesis. *International Geology Review* **53**, 656–76.
ZHANG, G. W., DONG, Y. P., LAI, S. C., GUO, A. L., MENG, Q. R., LIU, S. F., CHEN, S. Y., YAO, A. P., ZHANG, Z. Q., PEI, X. Z. & LI, S. Z. 2004. Mianlue tectonic zone and Mianlue suture zone on southern margin of Qinling-Dabie orogenic belt. *Science in China Series D: Earth Sciences* **47**, 300–16.
ZHANG, H. F., JIN, L. L., ZHANG, L., HARRIS, N., ZHOU, L., HU, S. H. & ZHANG, B. R. 2007. Geochemical and Pb-Sr-Nd isotopic compositions of granitoids from western Qinling belt: constraints on basement nature and tectonic

https://doi.org/10.1017/S0016756812000283 Published online by Cambridge University Press

affinity. *Science in China Series D: Earth Sciences* **50**, 184–96.

ZHANG, Z. H. & MAO, J. W. 2004. Fluid inclusions of orogenic gold deposits in the Zhongchuan Area, Western Qinling and their geological significance. *Acta Geologica Sinica* **78**, 481–91.

ZHANG, C. L., WANG, T. & WANG, X. X. 2008. Origin and tectonic setting of the Early Mesozoic granitoids in Qinling Orogenic Belt. *Geological Journal of China Universities* **14**, 304–16 (in Chinese with English abstract).

ZHANG, Q., YIN, X. M., YIN, Y., JIN, W. J., WANG, Y. L. & ZHAO, Y. Q. 2009. Issues on metallogenesis and prospecting of gold and copper deposits related to adakite and Himalayan type granite in west Qinling. *Acta Petrologica Sinica* **25**, 3103–22 (in Chinese with English abstract).

ZHANG, G. W., ZHANG, Z. Q. & DONG, Y. P. 1995. Nature of main tectono-lithostratigraphic units of the Qinling orogen: implications for the tectonic evolution. *Acta Geologica Sinica* **11**, 101–14 (in Chinese with English abstract).

ZHANG, C. L., ZHANG, G. W., YAN, Y. X. & WANG, Y. 2005. Origin and dynamic significance of Guangtoushan granitic plutons to the north of Mianlue zone in southern Qinling. *Acta Petrologica Sinica* **21**, 711–20 (in Chinese with English abstract).

ZHANG, G. W., ZHANG, B. R., YUAN, X. C. & XIAO, Q. H. 2001. *Qinling Orogenic Belt and Continental Dynamics*. Beijing: Science Press, 806 pp. (in Chinese).

ZHANG, S. B., ZHENG, Y. F., WU, Y. B., ZHAO, Z. F., GAO, S. & WU, F. Y. 2006. Zircon U-Pb age and Hf-O isotope evidence for Paleoproterozoic metamorphic event in South China. *Precambrian Research* **151**, 265–88.

ZHENG, Y. F. 2008. A perspective view on ultrahigh-pressure metamorphism and continental collision in the Dabie-Sulu orogenic belt. *Chinese Science Bulletin* **53**, 3081–104.

ZHENG, J. P., GRIFFIN, W. L., SUN, M., O'REILLY, S. Y., ZHANG, H. F., ZHOU, H. W., XIAO, L., TANG, H. Y. & ZHANG, Z. H. 2010. Tectonic affinity of the west Qinling terrane (central China): North China or Yangtze? *Tectonics* **29**, TC2009, doi: 10.1029/2008TC002428.

ZHENG, Y. F. & ZHANG, S. B. 2007. Formation and evolution of Precambrian continental crust in South China. *Chinese Science Bulletin* **52**, 1–12.

ZHENG, D. W., ZHANG, P. Z., WAN, J. L., LI, D. M., WANG, F., YUAN, D. Y. & ZHANG, G. L. 2004. The $^{40}Ar/^{39}Ar$, fission track evidence of Mesozoic tectonic in northern margin of west Qinling mountain. *Acta Petrologica Sinica* **20**, 697–706 (in Chinese with English abstract).

ZHOU, T. H., GOLDFARB, R. J. & PHILLIPS, G. N. 2002. Tectonics and distribution of gold deposits in China – an overview. *Mineralium Deposita* **37**, 249–82.

ZHOU, Z. J., QIN, Y., LIN, Z. W., WANG, L. X. & WANG, Z. Q. 2011. Study of fluid inclusion characteristic and genetic type of the Huachanggou gold deposit, West Qinling Orogen. *Acta Petrologica Sinica* **27**, 1311–326 (in Chinese with English abstract).

ZHU, L. M., DING, Z. J., YAO, S. Z., ZHANG, G. W., SONG, S. G., QU, W. J., GUO, B. & LEE, B. 2009*a*. Ore-forming event and geodynamic setting of molybdenum deposit at Wenquan in Gansu Province, Western Qinling. *Chinese Science Bulletin* **54**, 2309–24.

ZHU, R. X., YANG, Z. Y., WU, H. N., MA, X. H., HUANG, B. C., MENG, Z. F. & FANG, D. J. 1998. Palaeomagnetic constraints on the tectonic history of the major blocks of China during the Phanerozoic. *Science in China Series D: Earth Sciences* **41**, 1–19.

ZHU, L. M., ZHANG, G. W., DING, Z. J., GUO, B., WANG, F. & LEE, B. 2011. Zircon U-Pb ages and geochemistry of the Wenquan Mo-bearing granitioids in Western Qinling, China: constraints on the geodynamic setting for the newly discovered Wenquan Mo deposit. *Ore Geology Reviews* **39**, 46–62.

ZHU, L. M., ZHANG, G. W., LEE, B., GUO, B., GONG, H. J., KANG, L. & LÜ, S. L. 2010. Zircon U-Pb dating and geochemical study of the Xianggou granite in the Ma'anqiao gold deposit and its relationship with gold mineralization. *Science China Earth Sciences* **53**, 220–40.

ZHU, L. M., ZHANG, G. W., LI, B., GUO, B., KANG, L. & LÜ, S. L. 2009*b*. Geology, isotope geochemistry and ore genesis of the Maanqiao gold deposit, Shanxi Province. *Acta Petrologica Sinica* **25**, 431–43 (in Chinese with English abstract).

ZIEGLER, P. A., VAN WEES, J. D. & CLOETINGH, S. 1998. Mechanical controls on collision-related compressional intraplate deformation. *Tectonophysics* **300**, 103–29.

https://doi.org/10.1017/S0016756812000283 Published online by Cambridge University Press